Dynamics of slow and fast landslides

Núria M. Pinyol[*], *Mauricio Alvarado*[†], *Luis M. Garcia*[*]

[*]*Department of Civil and Environmental Engineering. Universitat Politècnica de Catalunya.*

nuria.pinyol@upc.edu

[†] *School of Civil Engineering. University of Leeds*

Abstract

The paper discusses some factors that control the shearing soil behaviour and the dynamics of landslides: strain-, strain rate-, and temperature effects.

The strain rate effect on residual strength is discussed through shearing tests reported in the literature on saturated samples at velocities ranging from 10^{-5} mm/min to 10^{4} mm/min. Such range covers from very slow to very rapid landslides according to landslide classification. The analysis of available data is presented and provides a framework which helps to define the constitutive law and phenomena further selected for the landslide analyses.

Some recent experimental published works are also discussed to show the temperature effect on shear strength. It is concluded that temperature effects are strain-rate dependent. The available data on that is limited and it may have a relevant effect in shallow landslides in which the sliding surface suffers the influence of weather induced temperature changes.

The second part of the article focusses on the analysis of landslides including several factors affecting the available shearing strength of the soils involved in instabilities. The motion from triggering to the final re-established equilibrium of slow and rapid landslides is analyzed through academic and simple examples as well as documented real cases. Under some hypotheses to simplify the problems, governing equations are solved analytically or in a simple numerical way to facilitate the discussion and to perform sensitivity analyses. With the interest of evaluating more realistic cases, some simplified hypotheses are relaxed and complex geometries and conditions are taken into account through numerical modeling. The material point method is selected. The MPM numerical codes, recently developed, can deal with strain- and strain-rate dependent shearing strength and include coupled effects likely developed during motion in landslides.

Strain-softening of shear strength causing progressive phenomenon is firstly discussed not only because of its effect on triggering first failures, but also for the estimation of landslide run-out. Compound landslides are specifically analyzed to discuss the progressive phenomena developed along internal shearing planes. Peak and residual strength envelopes control the landslide acceleration. The magnitude of the strength drop correlates well with the run-out.

Including a strain rate hardening component to the strength allows the assessment of creeping landslides. Weakening phenomena inducing the acceleration of landslides are not directly included as an intrinsic feature. The loss of residual strength that may lead to a rapid landslide is explained by invoking thermal water pressurization. Both effects, strain rate hardening and hydro-thermal coupled weakening, are probably present during motion. Soil properties, landslide features, and external conditions will determine the landslide motion. This interaction is discussed in terms of run-out and velocity of landslides subjected to static conditions, as well as seismic actions.

1 INTRODUCTION

Fictional strength evolution of materials involved in landslides controls the triggering, motion and deposition of the unstable mass. In this article, we focus on the effect of the strength on landslides that can be considered as a mass sliding on a well-defined slip surface, which undergoes internal shearing.

Experimental data indicate that the available residual strength changes significantly depending on several features, as well as coupled effects (deformations, pore pressure and temperature) that take place, especially, at large displacements and velocities. The strength offered by a soil subjected to shearing is the of internal forces at the grain level. Therefore, basic properties such as mineralogy, particle shape and size and index properties (Lupini et al., 1981; Mesri and Cepeda-Diaz, 1986; Di Maio and Fenelli, 1994; Stark and Eid, 1994, 1997; Tiwari and Marui, 2005; Stark and Hussain, 2013;), as well as chemical and rheological properties of the fluids filling the voids (Kenney, 1967; Moore, 1991; Di Maio and Fenelli, 1994; Tiwari et al., 2005; Scaringi and Di Maio, 2016) will determine the available shearing strength.

Given a soil defined by its intrinsic properties, the shearing resistance depends significantly on several factors that may change during landslide motions such as normal stresses (Bishop et al. 1967, 1971; Chandler, 1977; Stark and Eid, 1997, Toyota et al., 2009), accumulated displacement (Lemos et al., 1985; Stark and Eid, 1994; Toyota et al., 2009;), shear strain rate (Tika et al. 1996,1999, Scaringi and Di Maio, 2016, Scaringi et al., 2018, among others) and temperature (Shibasaki et al. 2017). The observed dependence is, often, complex and far away from simple linear relationships that are often assumed when employing the Mohr-Coulomb law. The effects of strain, strain rate and temperature will be discussed in this article.

The effect of the accumulated displacement has a clear and well-known effect on first failures. The loss of strength due to the accumulated plastic strains observed in the constitutive response of the soils leads to progressive failure phenomenon (Terzaghi and Peck, 1948; Taylor, 1948; Skempton, 1964; Bjerrum and Bishop, 1967; Palmer and Rice, 1973; Stark and Eid, 1994; and Puzrin and Gemonovich, 2005). Slope failures controlled by the mechanism of progressive failure are widely recognized and analyzed in the literature. (Potts et al., 1990, 1997; Gens and Alonso, 2006; Troncone, 2005, and Troncone et al., 2014). On the contrary, the effect of the strain-softening on the post-failure behavior is not so much explored.

The strain-rate dependence of strength is often invoked to explain the motion of observed landslides. Once triggered, the residual shear strength and its evolution control the kinematics of the landslide motion (Leroueil, 2001; Wang et al., 2010; Lucas et al., 2014; Alonso et al., 2016). Increments of the strength -strengthening behavior- during motion might prevent the acceleration of the unstable mass and avoid catastrophic failures. On the contrary, weakening involves the loss of strength, which may lead to the acceleration of landslides.

The intrinsic effect of temperature on shear strength probably has a more limited effect on landslides and the literature on this topic is not so extensive as it is in other factors affecting the strength. Shibasaki *et al*. (2016) discuss, based on documented cases, that shallow active landslides, less than 10 m deep, began to move during cold seasons. The observed response could not be explained solely by fluctuation in pore water pressure (groundwater level). They infer that the changed ground temperature might play a key role on the destabilization of marginally stable slopes. In particular, they focus in the case of Touge landslide. It can be observed in Figure 1 that the periods in which the landslide is active (highlighted in grey) and displacements were registered, coincide with decreases of temperature. Changes in pore water pressure during these periods are not relevant except in the third period, when the displacement are higher. Additional experimentally-based investigations, discussed in more detail in this article, were also carried out to confirm at laboratory scale the sensitivity of strength to the temperature (Shibasaki et al. 2017).

On the other hand, the available strength is also controlled by coupled effects that induce a variation of the pore water pressure during motion. In this category, we can include the volumetric strains induced by shearing (contracting and dilatant response). Undrained mechanisms of static liquefaction lead to flow-like

landslides which may lead the liquefaction. Hung et al (2001), Picarelli et al. (2008), Sassa (2000) and Ng (2009) discuss this phenomenon and examples of real cases are presented, for instance, by Wang et al. (2002) and Cascini et al. (2010).

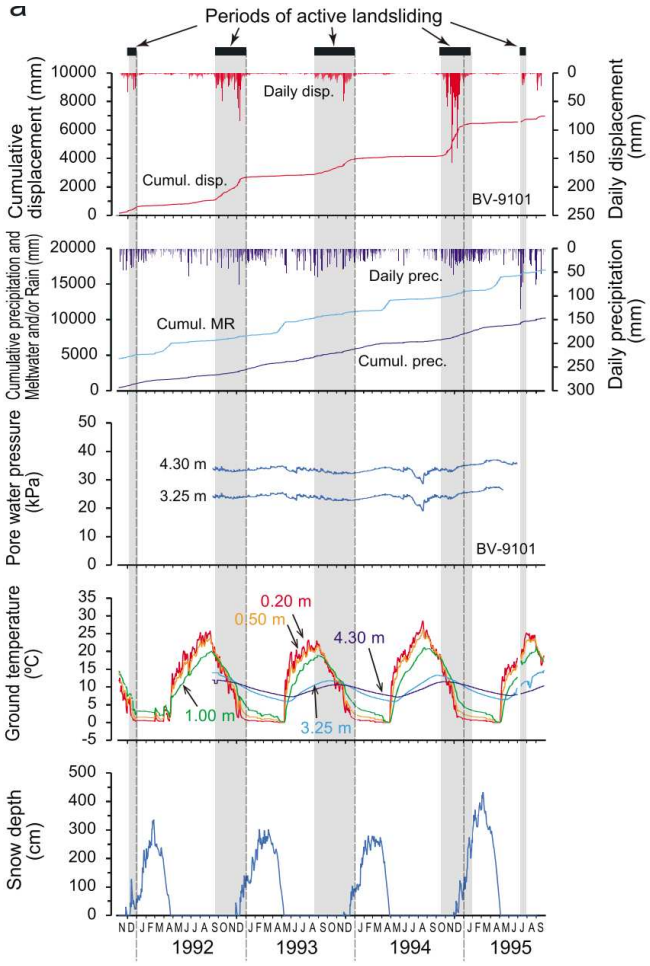

Figure 1. Touge landslide. Landslide movement and hydrological and meteorological conditions for 54 years. (Shibasaki et al., 2016).

Another coupled effects controlling the slide velocity are the thermal pressurization due to frictional work dissipation in heat (see Alonso et al., 2016 for references).

This article firstly presents a compilation of published experimental evidence on the complex response of shearing strength affected by several factors. This section is an introduction for the discussion about the constitutive law and phenomena further selected in landslide analyses. In particular, we discuss strain rate and temperature effects. The discussion focusses on the phenomena invoked to explain the observed behaviour, distinguishing between the intrinsic causes related to physical fundamentals of the frictional process at the micro level and, in contrast, other coupled phenomena.

The second part of this article quantifies the effect of strengthening and weakening of strength behavior on the soil response at failure and post-failure stage. This analysis will be carried out through the solution the governing equations and constitutive models including non-constant frictional strength laws.

The analysis of academic examples presented in this article allows developing analytical solutions and performing sensitivity analysis to raise practical conclusions. Complex cases are also presented to simulate real landslides through two-dimensional numerical analysis using the material point method (MPM) (Sulsky et al., 1994). This numerical tool is suitable to analyze the landslides from triggering to deposition. Using a double discretization into material points and computational mesh, the method is capable of simulating large displacements overcoming mesh problems that restrict the use of the standard finite element method in these large-displacement problems. Recent applications of MPM on landslides are described in Fern et al. (2018).

In particular, two MPM numerical codes are used for modeling landslides using a single-layer approach (Fern et al., 2018). The first one is GEOPART code (Zabala *et al*. 2004; Zabala and Alonso 2011). It was a pioneer MPM code for geotechnical applications. Pinyol et al. (2018) presented the extension of GEOPART to solve non-isothermal problems in unsaturated soils including the dissipation of frictional work during shearing for its application in landslides. Thermal-hydro-mechanical (THM) coupled problems are analyzed with this code. The second code used in the examples presented in this article is Anura3D developed by MPM Research Community (www.anura3d.com). Although the code is able to deal with 3-phase materials (Yerro *et al*., 2015) only a 2-phase approach presented here.

Through these examples, the strain-softening, reduction of shear strength due to plastic strains, is first evaluated. The examples described highlight the relevance of the strength degradation and the development of progressive failures on the basal sliding surface as well as on internal shearing surfaces.

Strain-rate hardening behavior is later introduced in an analytical analysis of two

creeping landslides simplified to planar geometries. The well documented Alverà (Angeli *et al*., 1999) and Vallcebre (Corominas *et al*., 2005) landslides were selected. In both cases, the loss of stable conditions is caused by increments of the water level according to field measurement.

Then, the case of Canelles landslide (Pinyol et al. 2018) is discussed in detail focusing on the interaction between two phenomena: strain-rate hardening and pore water pressurization-induced weakening.

The effect of the strain-rate dependent strength is finally evaluated for the case of earthquake-induced landslides. The dynamic analysis of landslide subjected to seismic action is first carried out in terms of permanent displacement analysis following the method developed by Newmark (1965). It is a relatively simple method (but more realistic than pseudo-static method) to quantify the seismic effects on slopes without developing overly complex stress-deformation analysis. Newmark's method models a landslide as a rigid block that slides on an inclined plane subjected to an earthquake ground acceleration at the base of the block during an interval of time. The block, taking into account the initial conditions such as the inclination of the sliding surface, pore water pressure, and basal resistance, has a known yield or critical acceleration that is required to initiate the sliding. Given an earthquake of interest, characterized by the acceleration-history of the ground, those parts of the acceleration records that exceed the critical acceleration are integrated to obtain the velocity-time history of the block. A second integration provides the accumulated displacement. The consequences of the earthquake on the landslide can be then judged in terms of accumulated displacements.

The Newmark's method is applied to planar slides inspired in a real case analyzed at the design stage in which the strain rate effects of the dynamic shearing resistant to the basal surface are included. This analysis aims to evaluate the effect on the accumulated displacement for a realistic range of frictional strength increments.

The article ends with the academic MPM numerical analysis of a saturated slope subjected to an earthquake. The response of the slope is evaluated using a dynamic THM analysis, which includes a strain and strain-rate dependent constitutive law for the strength.

2 EXPERIMENTAL EVIDENCES

2.1 Strain and strain rate effects

A large number of publications evaluate the residual shear-rate-dependent behavior by imposing a wide range of values corresponding to extremely slow landslides. The different kinds of experimental tests (ring shear and shear box and rotatory apparatuses) exhibit a complex response. Tika et al. (1996) present a thorough discussion on this. Figure 2 shows a schematic representation of the observed behavior according to this contribution corroborated later by other authors. The initial available strength corresponds to the slow residual friction strength observed at slow shearing rate. Increment of the shear velocity involves an increment of the strength, whose magnitude depends on the rate of displacement, at a negligibly small displacement. A further increase in strength is reached for increasing shearing rate, called fast peak strength. After reaching a peak, the strength drops with further fast-displacement to a value which may be higher (positive effect of strain rate), lower (negative effect) or equal (neutral effect) than the slow drained residual strength. If a final stage is applied in which the shearing velocity reduces, a slow peak strength greater than the slow drained residual strength measured at the beginning of the test is measured.

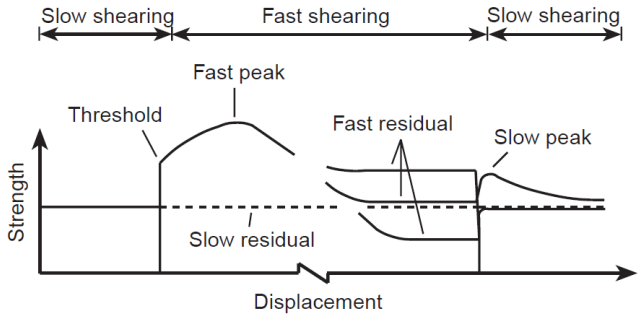

Figure 2 Schematic representation of the observed rate-dependent phenomena for residual strength (Tika et al., 1996).

Figure 3 collects the fast residual strength available in the literature carried out on saturated samples.

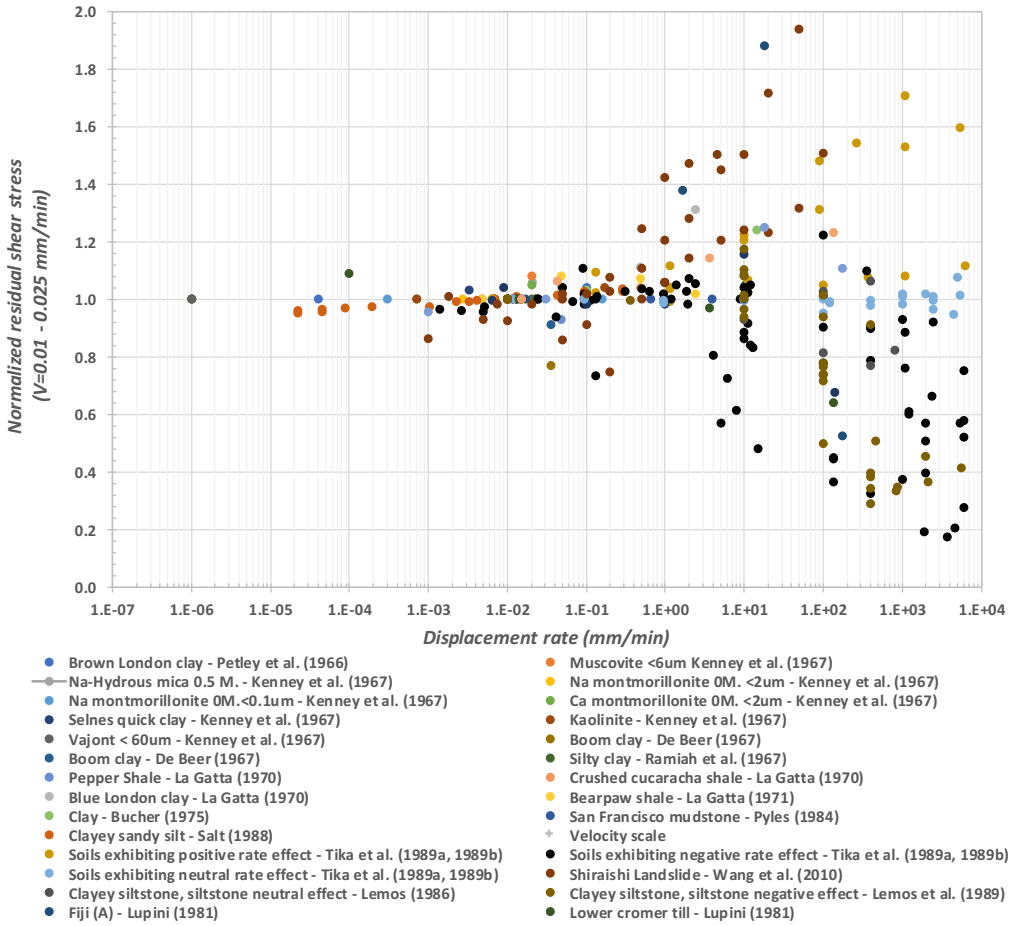

(a)

Figure 3 Residual shear strength normalized by the value obtained at low displacement rate against the displacement rate.

In Figure 4 the data are classified in terms of fine content (CF). This property has been selected to discuss the result taking into account that CF determines the intrinsic features controlling the frictional strength, although other properties are also relevant. According to these results, there is no general clear trend of exhibiting negative, positive or neutral shear rate effects depending on the clay fraction. However, for the discussion is it interesting to separate the results in the manner done in Figure 4. The Varnes' classification (updated by Hungr et al., 2014) is indicated and correlated with the displacement rate. Although the phenomena occurring at the shear band level is complex, including dilatancy or contraction, water flow, the disordering of particles, crushing of granular particles, among others, we will try to evaluate general trends.

What is observed is that the effect of the displacement rate manifests when this exceeds a certain value around 10^{-3}-10^{-2} mm/min, which corresponds to a moderate landslide velocity according to the Varnes classification. Therefore, there is a critical low velocity below which the strain rate effects are negligible. Tika et al. (1996) observed that this value depends on the soil but also on the normal stress applied.

For shear velocity values higher than 100 mm/min, negative rate effect is observed in all of the cases except in the results presented in Tika et al. (1989b) in fine soil samples with a CF higher than 60%. For lower values of shear velocity but higher than the critical low values, almost of all the tests indicate a positive effect except in the case of the results reported by Tika et al (1989a and b). Therefore, in general terms, we could conclude that, above a certain critical low value, increments of the shear velocity lead to increments of residual shear strength with respect to the value associated to slow velocities. This

positive effect, when observed, increases gradually with the velocity. In some materials, the strain-rate effect change to negative when velocity is higher than a critical high value. In some cases, this drop is abrupt as it is observed in tests on samples with CF lower than 40% (Figure 4c and d).

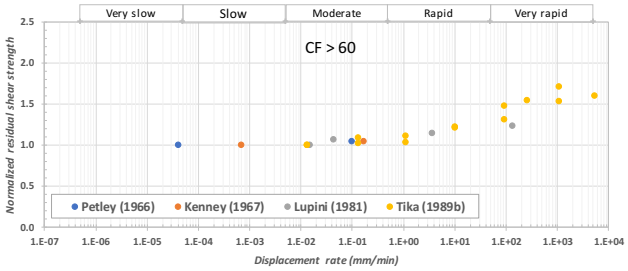

(a)

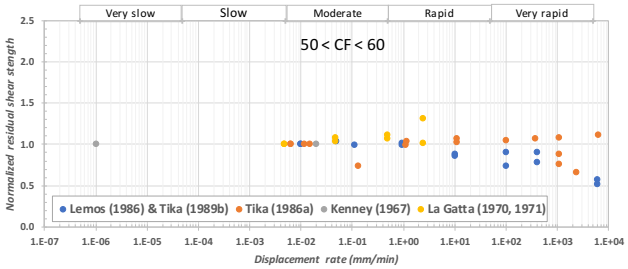

(b)

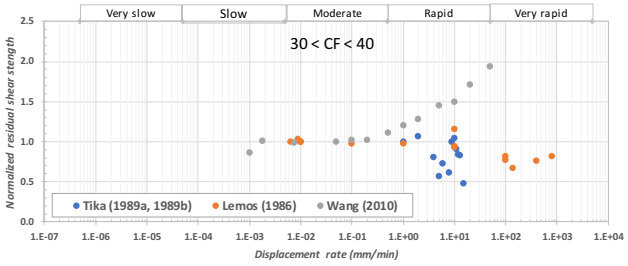

(c)

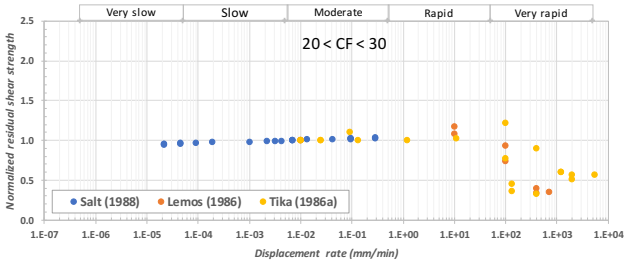

(d)

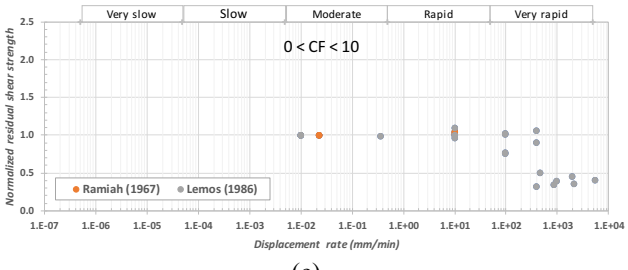

(e)

Figure 4 Residual shear strength normalized by the value obtained at low displacement rate (v=0.01-0.025 mm/min) against the displacement rate for different values of fine content (CF).

Several discussions on the causes leading to this observed behavior is given in the articles that report the experiments. Some of them support their explanation on the texture and sliding surface geometry. The shearing soil response depends on the intrinsic features that affect the fundamental phenomenon of friction and how particles interact at the shear band level. We can include the coefficient of inter-particle friction, index properties, grading of granular phase, shape of rotund particles and relative size of rotund and plate particles. During shearing, the structure of the soil reached at residual condition may change at fast shearing, because increments of shear strain rate may disorder the particles.

Fast shearing may involve an increment of the void ratio of the shear zone. This dilation may induce the rapid penetration of water, when it is available, which leads to a loss of strength observed in the test. Therefore, the fast shearing does not take place at constant water content, a situation which will have a relevant effect because the shear band soil becomes a looser flow structure. As Tika et al. (1996) state free water may be available in the field in case of fissured clay, but it is unlikely to be present in case of an intact one. This means that the loss of strength observed in the experiments when the rate of displacements increases, beyond critical values, may not develop in the soil unless there is an internal supply of water along the shear surface during the fast sliding.

The loss of strength induced by the entrance of water can be understood as a coupled phenomenon which is a consequence of the fast shearing inducing dilation of the soil. Excess pore water pressure generation during fast shearing is also a coupled effect that may control the shearing strength. The question is to know if this thermal interaction may play an important role in the experiments to explain the negative effect of the strain rate in fast sliding. Measurements of pore water pressure and temperature during fast sliding were reported by Tika et al. (1996) using an instrumented rough glass interface. The conclusion was that the measured pore water pressure during fast shearing cannot explain the reduction in strength below the slow residual values. Measured values of temperature were

relatively small and, according to theoretical analysis, were not enough to induce the required excess pore water pressure observed.

This aspect is discussed here in more detail. Consider a fast shear test as a representative example in which a shearing velocity, *v*, is applied on the loaded sample (σ_n). This test would correspond to a shear test of a block moving over a fixed surface at a constant velocity. This is a simplified analysis to evaluate the shear test results discussed. The temperature (θ) and excess pore water pressure generated (u_w) during this representative test can be calculated by applying the governing equations: water and solid mass balance, energy balance and constitutive equation defining the shear strength. In the case of neglecting the dissipation of water pressure and heat flow during the test, the mass balance equation reduces to:

$$-\beta_{soil}\frac{\partial\theta(t)}{\partial t}+m_{soil}\frac{\partial u_w(t)}{\partial t}=0 \qquad (1)$$

where $\beta_{soil}=n\beta_w+(1-n)\beta_s$ and $m_{soil}=m_v+\alpha_w$. β_s and β_w is the thermal dilation coefficient of solid and water, respectively. α_w the water volumetric compressibility and m_v the compressibility coefficient of the soil. The temperature varies due to the heat generated and as a function of the specific heat of the soil, c_m:

$$\frac{\partial\theta(t)}{\partial t}=\frac{H(t)}{\rho c_m} \qquad (2)$$

where $\rho c_m=(1-n)\rho_s c_s+n\rho_w c_w$ is expressed in terms of specific heat of solid and water (c_w, c_s) and their density (ρ_w, ρ_s).

The heat generated in time is assumed equal to the frictional work dissipated during sliding:

$$H=W=\frac{\tau_f v}{e} \qquad (3)$$

where *e* is the thickness of the shear band. These equations are developed in more detail for the case of the landslide in Alonso et al. (2010).

Combining previous equations, the time variation of excess pore water pressure becomes:

$$\frac{\mathrm{d}u_w(t)}{\mathrm{d}t}=\frac{\beta_{soil}\tan\varphi' v}{m_{soil}\rho c_m 2e}\left[\sigma_n-u_w(t)\right] \qquad (4)$$

that can be solved analytically:

$$u_w(t)=\sigma_n\left(1-e^{-\frac{\beta_{soil}\tan\varphi' v}{m_{soil}\rho c_m 2e}t}\right) \qquad (5)$$

Notice that this equation indicates that the increment of the pore water pressure evolves exponentially until it reaches a value equivalent to the total stress applied, which results in the total loss of the effective strength.

Equation (5) is applied for a sample of a soil exhibiting a residual strength of 15º of friction angle subjected to a normal stress σ_n=500 kPa. The thickness of the shear band, which has a significant effect (Alonso et al., 2016), is assumed to be 1 mm. The remaining parameters are indicated in Table 1. The thermal conductivity indicated in the table is not considered here because heat flow is assumed to be zero (adiabatic). Figure 5 shows the analytically computed pore water pressure, temperature and strength during the test. The results are plot in terms of displacement and, therefore, they do not depend on the imposed velocity. For low velocities, large displacement has no sense because such large displacement would require a long time and the impervious and adiabatic conditions assumed in the analytical development would be unrealistic. A maximum displacement equal of 1 m has been selected to plot the results. Displacements in reported ring shear tests in the literature typically range from 100 to 800 mm.

Table 1 Model parameters for water and solid in the THM analysis.

Parameter	Symbol	Value	Units
Water			
Density	ρ_w	1000	kg/m^3
Coefficient of compressibility	α_w	$5\cdot10^{-10}$	1/Pa
Thermal expansion coefficient	β_w	$3.42\cdot10^{-4}$	1/ºC
Specific heat	c_w	$4.19\cdot10^{-3}$	J/(kg ºC)
Thermal conductivity	Γ	0.580	J/(m s ºC)
Solid particles			
Density	ρ_s	2700	kg/m^3
Thermal expansion coefficient	β_s	$3.0\cdot10^{-5}$	1/ºC
Specific heat	c_s	$8.37\cdot10^{2}$	J/(kg ºC)
Thermal conductivity	Γ	0.375	J/(m s ºC)

Notice that in case of a test at 1000 mm/min during 15 seconds, the accumulated displacement

is 250 mm and the effective frictional angle drops from 15º to 11º, which corresponds to 70% of the initial strength. These values seem to be enough relevant to take them into account in the explanation of the strength weakening observed during fast tests on saturated soils. The results depend on the selected parametres. Figure 5 also shows the results for the case of a thicker shear band. The thermal effect in this case is significantly lower.

It is important to highlight that these results are computed for undrained and adiabatic conditions which may differ from real tests conditions.

2.2 Temperature effects

Since the pioneering contribution of Habib (1967) to explain the large and catastrophic acceleration of Vajont landslide, several contributions (Uriel Romero and Molina, 1977, Voigth and Faust, 1982; Vardoulakis, 2000, 2002, Veveakis et al. 2007; Goren and Aharonov; 2007, 2009; Pinyol and Alonso, 2010a,b, Goren et al., 2010, Cecinato et al., 2011, He et al., 2015, Alonso et al., 2016; Pinyol et al., 2018) delved into the loss of effective strength induced by friction on a shear band. None of these contributions mention the direct effect of the temperature on the shear strength apart from the coupled thermal effect that induces changes in pore water pressure. Probably the main reason is that, when coupled effects are relevant and significant increments of temperature are reached, the direct effect of temperature on the shear strength becomes negligible. However, changes in external temperature may affect notably the sliding surface of shallow active landslide. An example is presented in the Introduction section (Figure 1).

To quantify the temperature effects on frictional strength, it is convenient to evaluate the shear strength under different but constant temperatures to prevent the coupled effects. Shibasaki et al. (2017) present an interesting work on this topic.

Reference to previous works can be found in this contribution. Shibasaki et al. (2017) focus on the temperature effect on residual shear strength of soils with different contents of smectite (often present in landslides in Japan).

The effect was evaluated by carrying out ring shear tests. Under residual strength conditions, the sample was subjected to temperature-changes. Cooling experiments were preformed from a temperature lower than 45º to 5º approximately. At the final temperature, the residual friction strength was evaluated. Many of the tests were conducted at 200 kPa of normal stress and slow velocity (from 0.005 mm/min to 0.02 mm/min). Temperature effect was classified into negative (increments of temperature leads to a decrease of shear strength), positive (increments of temperature leads to increments of strength) and neutral (no effect) (Figure 6).

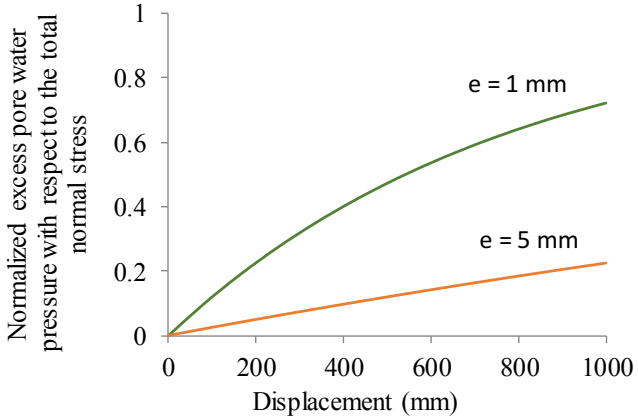

(a)

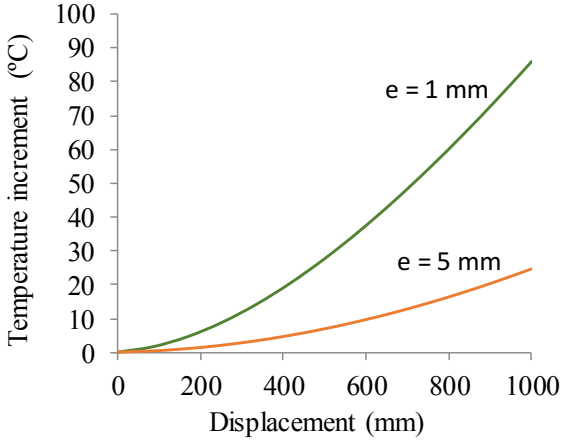

(b)

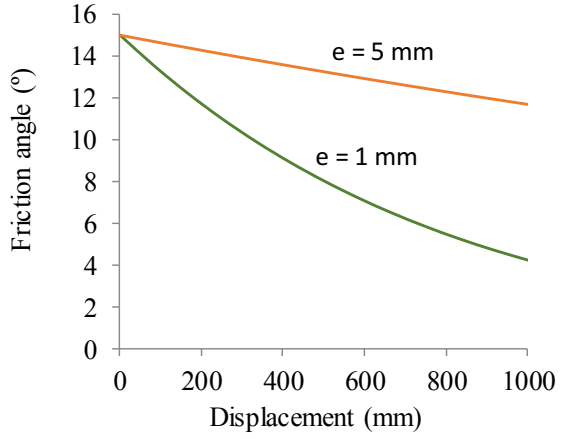

(c)

Figure 5 Analytical results of shearing test (preventing water and heat flow) for two values of shear band thickness: (a) Excess pore water pressure; (b) Temperature increment; (c) Equivalent friction angle and ratio of the effective friction strength over total stress normalized by the initial value when excess pore water pressure is zero.

They also evaluated the effect of temperature on the shearing-rate dependent strength. Figure 7a shows the results for samples with a smectite content of 36%. The samples were tested at different velocities. During shearing at a given strain rate, the temperature its dropped from the room temperature (around 20º) to a lower temperature (around 9º). The results are plotted in terms of the normalized strength variation with respect to the initial values for a 1ºC of change in temperature (referred to the secondary axis). The results indicates that:

(a) For a given temperature, the strain rate effect is positive for the range of velocities evaluated (0.001-0.05 mm/min).

(b) Temperature effect on residual strength changes from positive to negative with increasing shear rate.

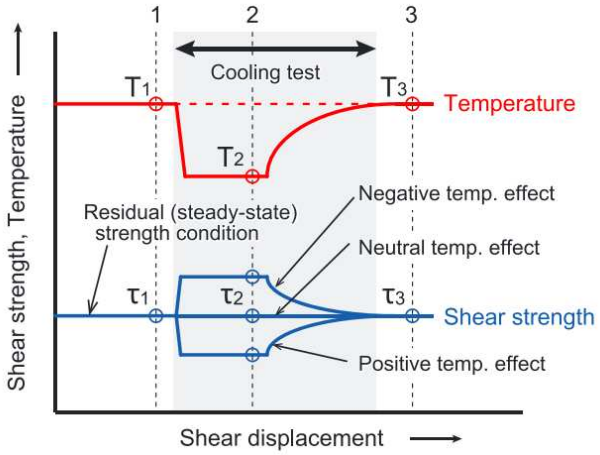

Figure 6. Schematic illustration of the effect of temperature change on residual frictional strength (Shibasaki et al., 2017).

The authors speculate about the reasons that explain such behavior for the case of rich-smectite samples. To do that, they refer to the analysis of forces developed at particle level during shearing presented by Hiatsune et al. (2009) and the effect of temperature.

It seems that the mineralogical composition of the samples has an important effect. When samples with low content of smectite are evaluated at low of displacement rates is not so high (Figure 7). The effect is finally plotted in Figure 8.

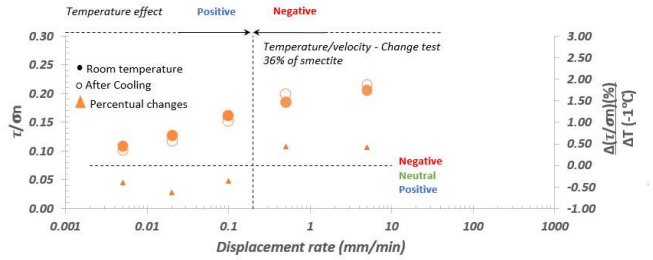

(a)

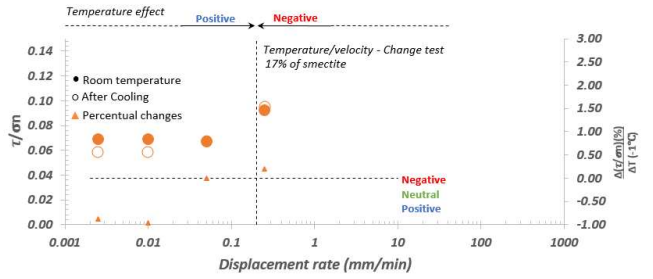

(b)

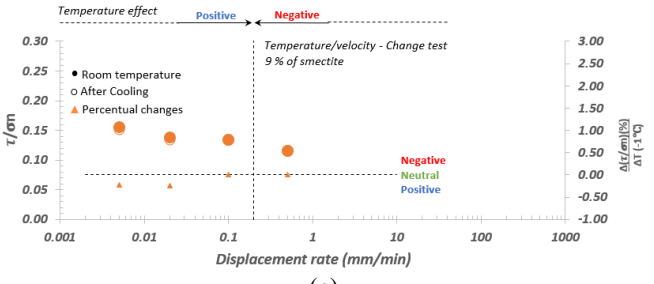

(c)

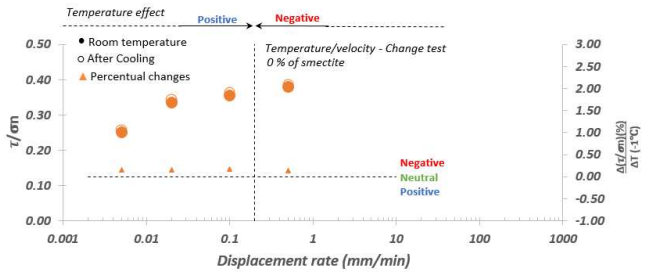

(d)

Figure 7. Effect of temperature on the strain-rate dependent strength (Shibasaki et al., 2017).

3 MODELLING LANDSLIDES

In this section, the changes in shear strength due to several factors and phenomena, some of them discussed previously and quantified in terms of frictional coefficient or friction angles, are included in the governing and constitutive equations and evaluated in cases of slope stability.

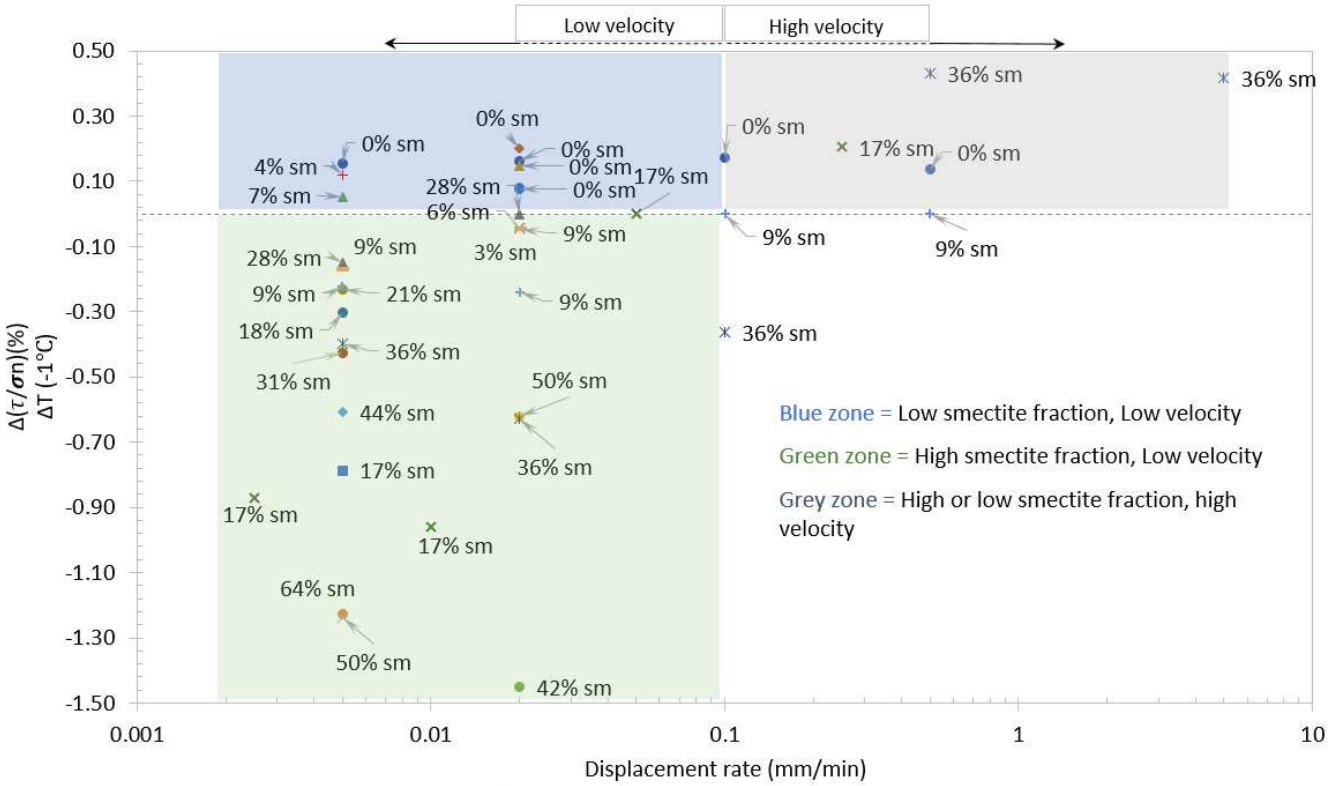

Figure 8. Effect of temperature on the strain-rate dependent strength for sample with different content of smectite (results from Shibasaki et al., 2017).

3.1 Strain dependence

Structural soils of medium to high-density exhibit a strain-softening behavior after peak conditions. This is, in particular, the case of high plasticity clays, where the drop from peak to residual strength envelopes is very significant. Rocks are also brittle materials for the typical range of stresses in geotechnical engineering. On the other hand, deviatoric loading, in frictional materials leads to the localization of shear strains in bands of small thickness. Strain-softening enhances localization. Therefore, in first time failures in strain-softening materials, one would expect the development of a well-defined failure surface where strength drops markedly as the shear strains accumulate. The failure process is non-homogeneous and develops progressively following a pattern controlled by the changing effective stress state and the soil/rock stiffness and strength properties.

Figure 10 shows the calculated stress path of a point (P2) which belongs to the final failure surface of the Selborne slope failure experiment (Cooper et al., 1998; Soga et al., 2016). The slope shown in Figure 10a was forced to fail under an increasing water pressure applied to the lower boundary of the model. The slope was excavated in on an overconsolidated high plasticity brittle clay. The peak and residual strength envelopes of the upper (weathered) and lower (undisturbed) layers of clay, shown in the figure, were determined in the triaxial test (Cooper et al., 1996, 1998).

A strain-softening Mohr-Coulom elastoplastic model characterizes the clay. Exponentially decaying functions of plastic shear strain define the effective cohesion and friction as follows,

$$c' = c'_{res} + \left(c'_{peak} - c'_{res}\right) \mathrm{e}^{-\eta \varepsilon_{eq}^{p}} \tag{6}$$

$$\phi' = \phi'_{res} + \left(\phi'_{peak} - \phi'_{res}\right) e^{-\eta \varepsilon_{eq}^{p}} \tag{7}$$

where subscripts r and p refer to residual and peak conditions. ε_{eq}^{p} is the generalized deviatoric plastic strain and η a parameter controlling the rate of strength decrease. The peak-cohesion values are 13 kPa and 4.7 kPa for the upper and lower layer and the residual values and drop to 4.7 kPa and 1 kPa respectively. The values of the peak and residual friction angle are 24.5º and 13.5º for the upper layer and 26º and 15º for the lower one.

At the start of the experiment (point A in Figure 9b) the soil remains in elastic conditions. As pore pressure increases, the effective mean stress

decreases and eventually reaches peak failure condition (Point B). Strain softening and the progressive increase in pore water pressure brings the stress state to residual conditions where it remains during the subsequent changes in geometry. The run-out of Selborne was close to 4 m for a slope having an initial height of 9 m. First-time failures in brittle soils are sudden events.

Soga et al. (2016) demonstrate that MPM modeling offers a good description of the static-dynamic transition of the time of failure. Anura3D is used for these calculations. Figure 10 shows the evolution in time of the mobilized friction angle on the three points distributed along the final failure surface. The attainment of peak conditions and the subsequent rapid drop to residual conditions is clearly shown in the three points.

However, at the scale of the calculated slope displacement, also shown in the figure, the slope remains essentially at rest except when Point D reaches the peak-residual rapid drop in strength. At that time (t=$t_{failure}$) the entire slope accelerates in the manner shown in Figure 11. Point P5 was the last one to reach peak conditions. Note also that the slope motion is not well characterized by a rapid body motion. This is a result of the necessary internal deformation of the soil above the sliding surface to achieve a kinematic compatibility of displacements.

The case of Selborne is an example of the relationship between soil brittleness and expected run-out if failure conditions develop.

This effect is discussed below in detail. The idea was to describe brittleness by the Bishop brittleness index:

$$I_B = \frac{\bar{\tau}_p - \bar{\tau}_r}{\bar{\tau}_p} \qquad (8)$$

where the bar over the peak and residual shear strength denotes the average along the failure surface. I_B, in the case of the drained analysis reported here, requires information on the effective normal stress acting on the failure surface. If, for a given slope geometry and a pre-defined failure triggering mechanism, run-out are calculated for different values of I_B, the suspected runout-I_B relationship could be established. Run-out is understood as the distance between the toe of the initial slope and the toe of the slope after failure once equilibrium is re-established. It may be different than the maximum displacement.

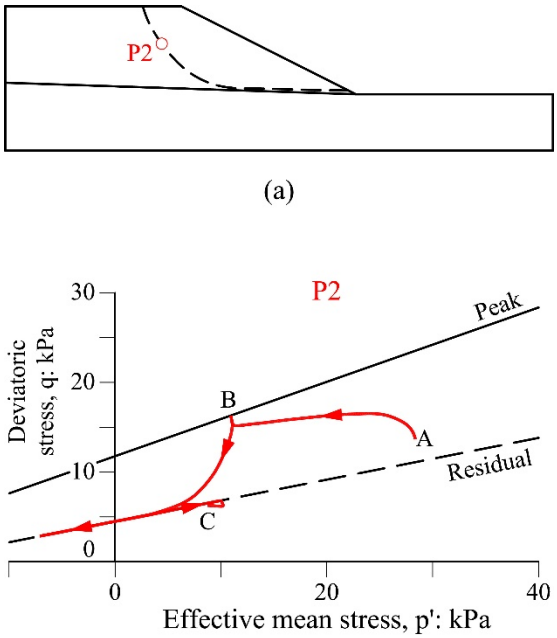

Figure 9 Computed stress path for point indicated in (a) (Soga et al. 2016).

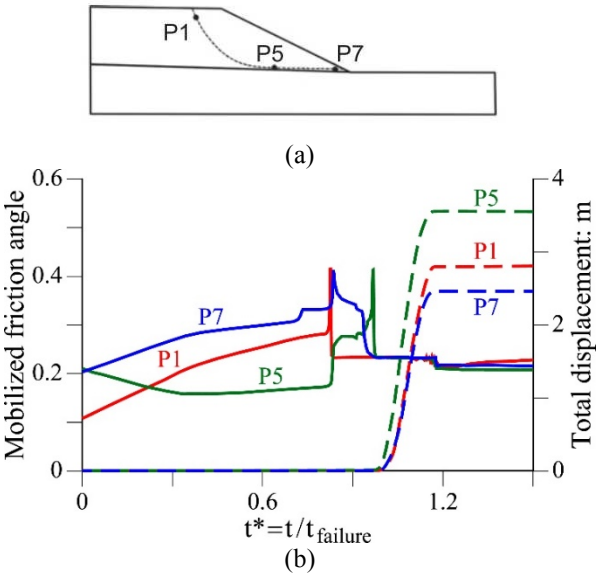

Figure 10 Evolution in time of the mobilized friction angle (solid lines) and total displacement (dashed lines) of the points initially indicated on the shear band (Soga et al., 2016).

The academic case was a simplification of the Selborne case (only one material was involved) and failure was induced by applying a constant water pressure applied on the lower boundary of the model.

For each one of the cases, solved the evolution of the stress, pore pressures, strains and, displacements provided a detailed picture of the phenomena developing inside the slope. Yerro et al. (2016) provides details. A convenient way to capture the progressive failure is to represent, for changing times, the mobilized friction angle along the failure surface. Figure 11a shows this information for times close to the slope failure. In this case, the failure progression from the toe towards the crest. The motion starts when the point at crest reaches residual strength. Note that the time evolution of the mobilized friction is a consequence of the transient flow imposed by the boundary water pressure. Progressive failure is not intrinsically related to time but reacts instantly to changes in effective stress. The evolution of the average mobilized friction angle along the failure surface is represented in Figure 11b. The average mobilized friction remains for all times far from the peak strength. When the last point (P1 in this case) reaches residual conditions, the slide accelerates.

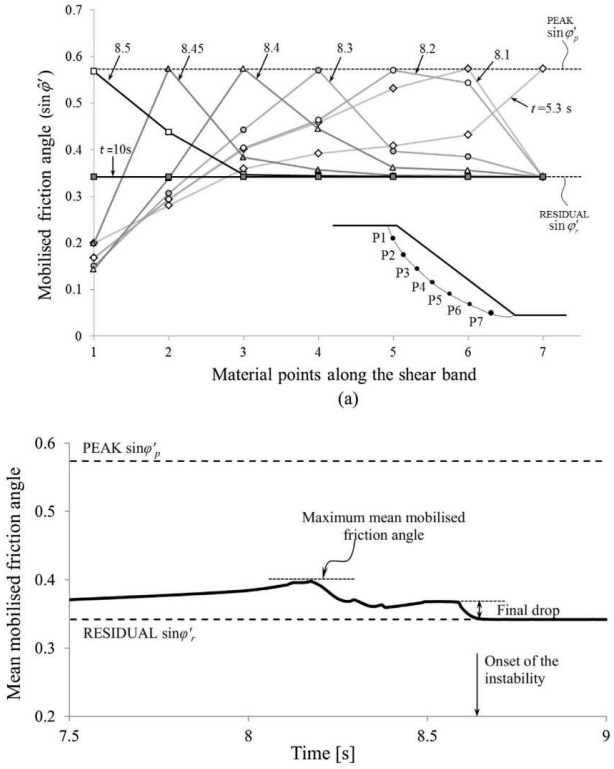

Figure 11. (a) Distribution of the mobilised friction angle along the initial shear band at different times; (b) Evolution of progressive failure in terms of mean mobilized friction angle. (Yerro et al., 2016).

Figure 12 collects the calculated run-out for cases characterized by a common peak strength (c'_p=5kPa, ϕ'_p=35º). Varying residual strength parameters leads to different IB values. The figures include results for two triggering causes: the boundary water pressure is either 40kPa and 70 kPa. A good correlation runout-IB is found in all cases. The figure indicates the minimum brittleness index required to set the slope in motion for the two boundary water pressure (I_B^{40} and I_B^{70}). It was also found that, even if the runout was well correlated with IB, the geometry of the failure surface (its depth in particular) was related to the specific values of the residual strength.

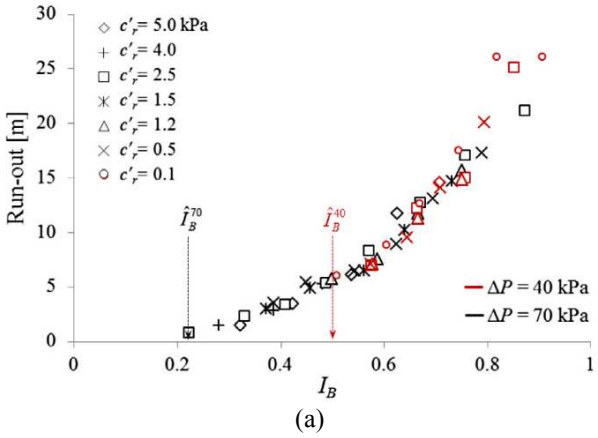

The unique relationship run-out IB is lost if the peaks strength parameters change substantially when compared with the previous case. Figure 12b shows a new relationship. In the case represented the increased values of c'_p and reduced value of ϕ'_p (9 kPa, 20º) leads to a deeper failure surface and an increased run-out.

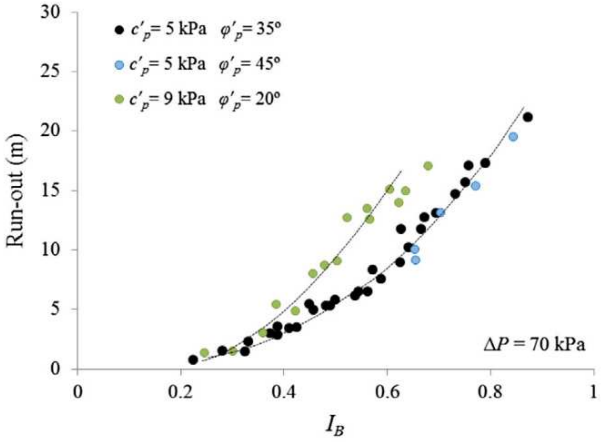

(b)

Figure 12. Computed run-out as a function of I_B. (a) All the cases with equal peak strength envelope; (b) Different peak strength envelope (Yerro et al., 2016).

3.1.1 Internal failure

Very often the sliding surface of landslide follows a clay or claystone layer, especially in the case of layered of rock formation. The rock above the failure surface may offer a significant resistance to deform in cases of kinematic non-compatibility of the entire mass. These slides are also known as "compound" landslides and Figure 13a shows some examples (Glanstonbury and Fell, 2008). Vajont landslide (schematically represented in Figure 13b) is also a good example. The figure shows a reconstruction of the interpreted initial cross-section of the left margin of Vajont valley and the situations after a paleolandslide that filled the valley. The figure is simplified and the failure surface is characterized by a sharp kink connecting the lower horizontal failure surface and the inclined one. The slide motion requires the internal shearing of the rock mass above the failure surface and the inclined one (Alonso et al., 2010 - Chapter 2). The slide motion requires the internal shearing of the rock mass above the failure surface. Shearing of the rock along a bisector plane of the lower dihedral angle makes the slide displacement kinematically admissible. A similar situation is found on the opposite side of the valley. The sheaded areas of the figure represent shared rock masses. Erosion by Vajont river modified later the valley geometry and prepared the scene for the recent 1963 failure.

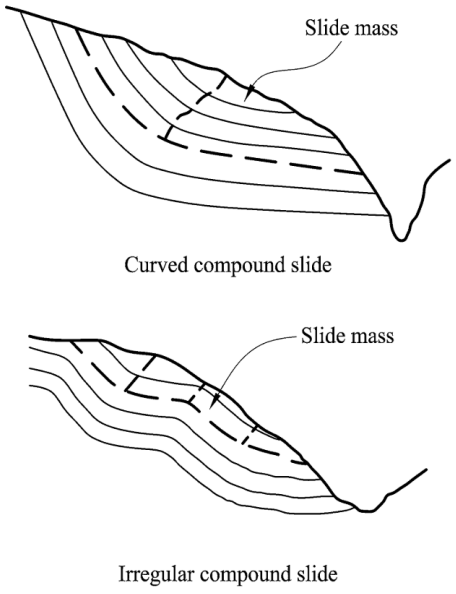

(a)

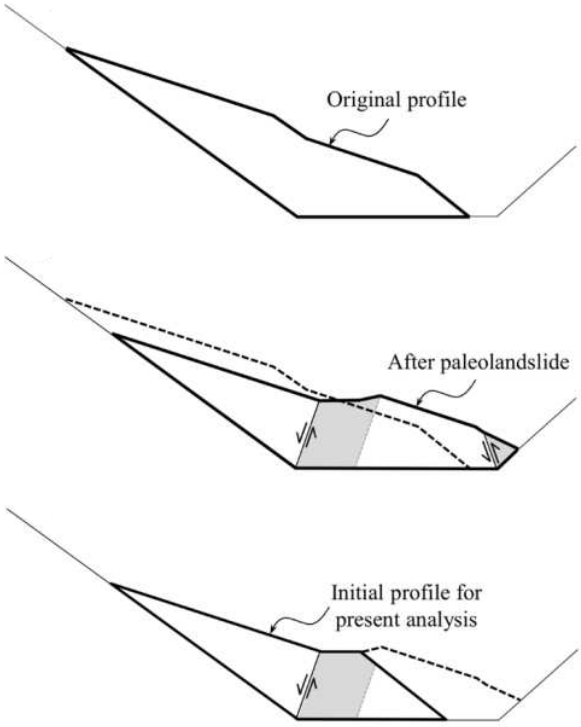

(b)

Figure 13. (a) Schematic illustration of the mechanisms of internally sheared compound slides (Glanstonbury and Fell, 2008); (b) Schematic representation of degradation of a compound landslide with motion (Yerro et al. 2016).

What follows is an exercise to quantify the role of internal shearing in Vajont landslide geometry when the rock mass above the sliding surface exhibits a strain softening behaviour. Vajont is a case of self-stabilizing geometry which is relatively common in folded rock stratification. Vajont is considered a reactivation of a previous

landslide and the sliding surface maintains a constant residual strength in the model developed.

The increase in the water level in the reservoir led to the instability of Vajont. This external action was reproduced in the model. Figure 14 shows the calculated runout in terms of water level of two widely spaced points on the terrain surface. They displace the same amount. The plot shows a very rapid increase in velocity when the reservoir level is 60 m above the lower level of the sliding surface (note the logarithmic scale of the horizontal axis). The initial application of the gravity loading was already capable of mobilizing the strength of the internal bisector plane. The water application of gravity loading was already capable of mobilizing the strength of this plane. Figure 15 shows the evolution of the mobilized friction along the bisector plane for increasing reservoir level. When the water height reached 69 m, the rapid drop in strength towards residual conditions triggered an accelerated motion.

Crossing the bisector plane(s) implies an irreversible shearing of the rock (Figure 16). The calculated thickness of the shearing bands is a consequence of the size of the computational mesh elements in MPM. They accumulate in the displaced rock as it crosses the shearing plane. This is also shown in plots representing the mobilized friction in the mid plane of the slide (Figure 17).

Figure 17a indicates the initial and final position of the material points selected to calculate the mobilized friction. Figure 17b shows the distribution of the mobilized friction in the selected moving point for different times. Also shown are the peak and residual strength limits. Initially, except for a zone around the bisector plane, which already reached residual conditions during gravity loading, the points remain elastic. As reservoir level increases and material points cross the shearing planes, peak and residual strength reach peak and residual conditions. When motion stops some point around MP's 5 and 6 unload and others, in the area of MP's 7 and 8, never experienced shearing.

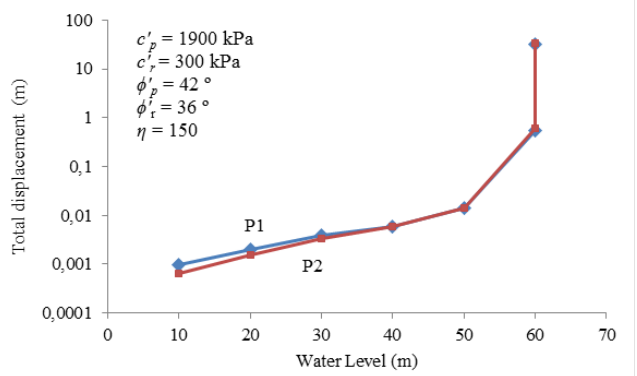

Figure 14. Run-out of the slide. Variation of accumulated displacement of two points located in the upper and middle part of the landslide surface (Yerro et al. 2016).

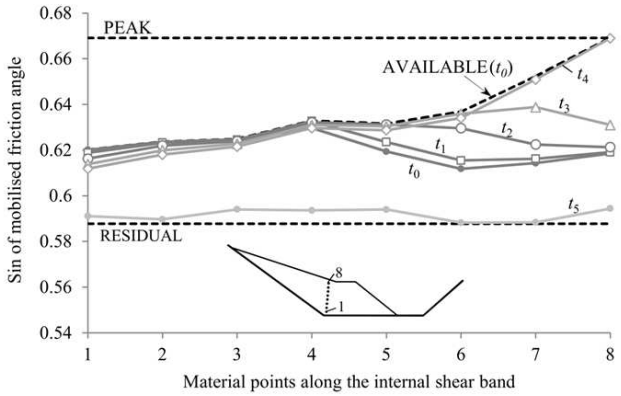

Figure 15. Progressive failure during increment of the water level submerging partially the landslide toe: at t_1, h_{w1} = 20 m; t_2, h_{w2} = 30 m; t_3, h_{w3} =4 0 m; t_4, h_{w4} = 50 m; t_5, h_{w5} = 60 m. (Yerro et al., 2016).

Figure 17a indicates the initial and final position of the material points selected to calculate the mobilized friction. Figure 17b shows the distribution of the mobilized friction in the selected moving point for different times. Also shown are the peak and residual strength limits. Initially, except for a zone around the bisector plane, which already reached residual conditions during gravity loading, the points remain elastic. As reservoir level increases and material points cross the shearing planes, peak and residual strength reach peak and residual conditions. When motion stops some point around MP's 5 and 6 unload and others, in the area of MP's 7 and 8, never experienced shearing.

If the sharp lower corner of the sliding surface becomes curved (a likely situation) the picture changes, and internal rock shearing becomes more involved.

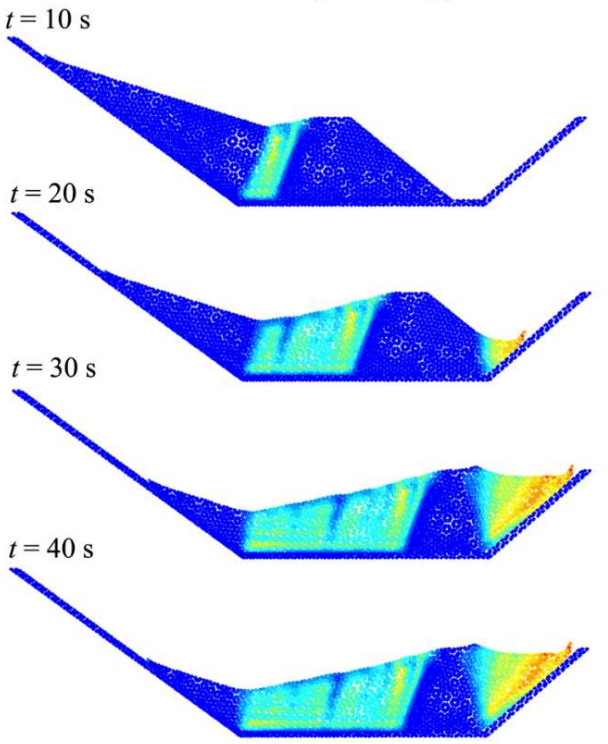

Figure 16. Accumulated deviatoric plastic strain at different times. Basal sliding friction equal to 0º (Yerro et al. 2016).

Minor details of the main failure surface (bumps, stepped geometries), which requires a more comprehensive structural characterization of the rock, will result in complex internal shearing.

An objective of the previous analysis was to check if a combination of a non-zero residual strength of the basal sliding surface and a progressive failure mechanism of the rock mass could explain the known runout and velocity of Vajont. The answer is that, even if a significant brittleness is assigned to the rock mass, field observation requires a zero basal shear strength.

The observed behavior of shear strength at the experimental scale is described theoretically through idealized models, formulated mathematically. The literature provides different approaches to simulate the velocity of landslides including the strain effects. Based on theories of "activation energy" at the level of microscopic contacts, Bowden and Tabor (1964), Mitchell (1976) and Rice (2001) obtain a law of friction that can be expressed as:

$$\mu = \frac{\tau}{\sigma} = f = f^* + \psi + A \ln \frac{v}{v^*} \qquad (9)$$

where f^* is the basic friction and ψ includes effects other than those associated with shearing velocity. The variable v^* is a reference velocity associated with the basic friction angle.

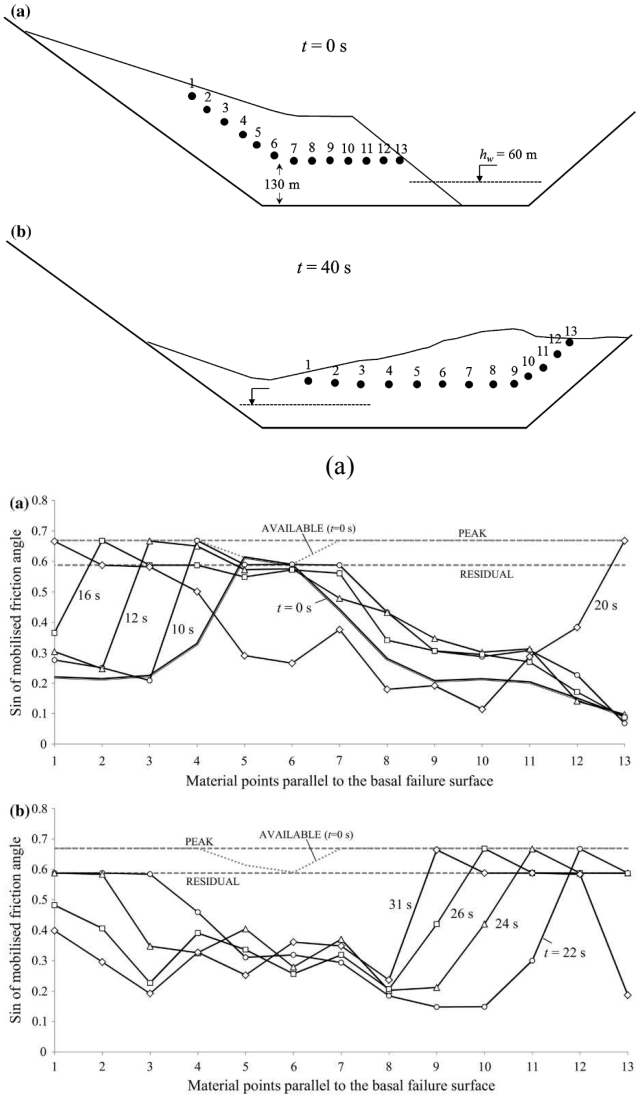

Figure 17. (a) Localization of 13 materials points during motion; (b) Rock degradation for basal friction angle equal to 0º (Yerro et al. 2016).

3.2 Strain-rate dependence

Equation (9) can be expressed in terms of friction angle as Wedage et al. (1998) proposed on the bases of experiments:

$$\tan\phi = \tan\phi_0 \left(1 + a \ln \frac{\varepsilon}{\varepsilon_0}\right) \qquad (10)$$

where a is a parameter controlling the effect of the strain rate ε dimensionless by a reference strain rate ε_0 normalized with the reference friction angle ϕ_0. Davis *et al*. (1993) presented alternative

proposals for the strain rate dependence of friction.

Ruina (1983) proposed similar friction laws winspired on direct shear tests on polished surfaces of rock and fault gouges

These approaches and equations are formulated to model intrinsic phenomena of soils that make the strength strain-dependent. They predict a linear increase of friction with the logarithm of shearing velocity, but they do not predict the negative effects supported by some experimental tests.

Empirical weakening velocity-displacement frictional laws, mainly inspired on high-velocity rotary shear experiments on fault gouges and landslide materials, are proposed following mathematical expression like (Mizogushi et al., 2007, Togo et al., 2009, 2011):

$$\mu(d,v) = \mu_{ss}(v)\left[\mu_p - \mu_{ss}(d,v)\right]\exp\left(\ln\left(\frac{0.05d}{D_c}\right)\right) \quad (11)$$

where the stress ratio μ is expressed in terms of the displacement, d, and the velocity, v, in terms of the peak stress ratio, μ_p, and the velocity-dependent friction coefficient $\mu_{ss}(d,v)$reached at the residual steady-state:

$$\mu_{ss}(v) = \mu_{ss}(v)\big|_{v=\infty} + \left[\mu_p - \mu_{ss}(v)\big|_{v=\infty}\right]\exp(v/v_c) \quad (12)$$

where $\mu_{ss}(v)\big|_{v=\infty}$is defined as the steady state friction coefficient when the shear velocity approaches infinity. v_c is a material constant and D_c corresponds to the increment of shear displacement required for a reduction of the friction coefficient of 95% (from μ_p to μ_{ss}) called slip weakening distance. Song et al. (2016) expressed this distance in terms of velocity. A complete program of experiments is required to calibrate these empirical laws.

Equation (11) and (12) try to reproduce the observed behaviour in experiments. They refer to the intrinsic behaviour of the shearing surface but they do not tell much about the physical phenomena controlling the loss of strength. For instance, relevant phenomenon such as pore fluid pressurization due to frictional heating in wet conditions are not considered. This phenomenon is invoked by Ujiie and Tsutsumi (2010) to explain the loss of strength on rotary shear tests. In this case, they carried out the tests in an apparatus capable of measuring the shear band temperature.

Pore fluid pressurization due to friction depends not only on the velocity but also on the normal stress and other variables. This is an important limitation of laws given in Equation (11) and (12) which only depend on velocity. These empirical expressions should only be applied in cases in which the normal stress, and the other variables controlling the fluid pressurization, remain constant and equal to conditions applied in the test used for its calibration. Otherwise, these laws are not correctly applied.

In this section, strain-rate hardening law discussed previously are incorporated in the analysis of landslides. Firstly, it is demonstrated that, by means of this law describing an intrinsic property, we are capable of predicting creeping behavior. However, they are not able to explain very fast slide acceleration starting from a dynamic equilibrium characterized by creep-like velocities.

In the approach presented in this section, slope instabilities are analyzed as a coupled thermo-hydro-mechanical problem to simulate the fluid pressurization by frictional work. This approach allows the landslide acceleration prediction. In these analyses, the strain rate hardening, which acts against the acceleration of the landslides, is also included. It is interesting to observe, through academic examples and sensitivity analysis in examples based on real cases, the interaction between both phenomena and the resulting evolution of landslide motion.

3.2.1 Creeping landslides

The following frictional law for the residual strength is used in terms of the sliding velocity, v:

$$\tan\phi_v = \tan\phi_{\min} + \left(\tan\phi_{\max} - \tan\phi_{\min}\right)\left(1 - e^{-\chi v}\right) \quad (13)$$

where the friction angle is controlled with parameter χ. The sub-index v indicates the dependence of the friction angle with the velocity. This law reproduces a gradual increment of strength with strain rate. Equation (10) is an example.

However, exponential laws (Eq. 13) are of interest to analytical developments. In fact, this kind of laws can explain the creeping motion observed on well-documented active landslide, in

contrast to the accelerated motion predicted by simple constant Mohr-Coulomb frictional laws.

For planar slides, defined by the sliding surface at a depth *D,* inclination β and a level of water parallel to the sliding surface at a height with respect to the sliding surface h_w, Newton's second law leads to the following differential equation defining the acceleration of the slide ($a = \frac{\mathrm{d}v}{\mathrm{d}t}$, where $\frac{\mathrm{d}v}{\mathrm{d}t}$ is the time derivative of the velocity):

$$\frac{\mathrm{d}v}{\mathrm{d}t} = g\left[\tan\beta - \left(1 - \frac{\gamma_w h_w}{\gamma_s D}\right)\tan\phi_v\right] \quad (14)$$

In Equation (2), γ_w and γ_s are the specific weights of water and *g* the gravity acceleration. For a given frictional law (Eq. (13)), a range a minimum (h_{w_min}) and maximum value (h_{w_max}) of water level can be established:

$$h_{w\_\min} = \frac{\gamma_s D}{\gamma_w}\left(1 - \frac{\tan\beta}{\tan\phi_{\min}}\right) \quad (15)$$

$$h_{w\_\max} = \frac{\gamma_s D}{\gamma_w}\left(1 - \frac{\tan\beta}{\tan\phi_{\max}}\right) \quad (16)$$

For values h_w ranging between h_{w_min} and h_{w_max}, the slide reaches the constant velocity expressed as:

$$v_{const} = -\frac{1}{\chi}\ln\left[\frac{\tan\phi_{\max} - \tan\phi_{v_{const}}}{\tan\phi_{\max} - \tan\phi_{\min}}\right] \quad (17)$$

where

$$\tan\phi_{v_{const}} = \tan\beta \Big/ \left(1 - \frac{\gamma_w h_w}{\gamma_s D}\right) \quad (18)$$

This analytical equation for constant creeping velocity (Eq. 17) is used to simulate the behavior of the two real cases. The first one is Alverà slide in Veneto, Italy (Angel et al., 1991; Deganutty and Gasparetto, 1991; Panizza et al. 1996) whose motion is measured and directly correlated with water level (Figure 19). It consists of alternating beds of sandstone, marl, and clay. This case was evaluated including the effect of the velocity by Angeli et al. (1996). In their approaches, the acceleration and deceleration of the moving mass is controlled by viscous resisting forces expressed in analogy with fluid mechanics and applied in flow-like landslides. The viscous response, which depends on the thickness of the layer in shearing, is reduced to a coefficient of dynamic viscosity. Viscosity is not easy to calibrate by laboratory tests.

The second case is Vallcebre landslide in the Pyrenees, Spain (Corominas et al., 2005). In this case, a clayey siltstone layer slides along the sliding surface located into fissured plastic shales.

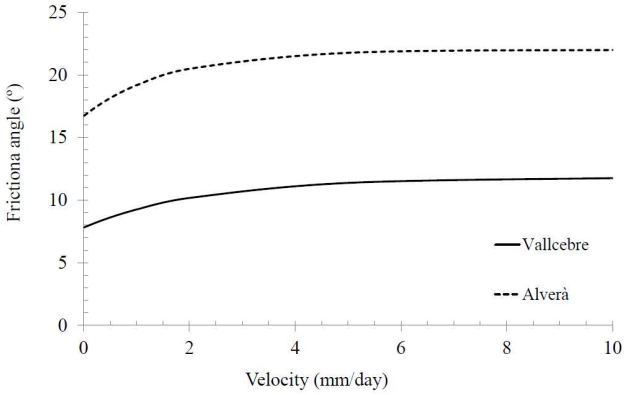

Figure 18. Variation of friction angle with sliding velocity.

For the analysis, both landslides are simplified as a planar landslide adopting the average thickness and average angle of inclination: 5 m and 11º for Alvera landslide and 15.4 m and 6.5º for Vallcebre.

The evolution of the water levels of each case has been introduced according to the available data (Figure 19a and Figure 20a). The minimum friction angle selected for modelling the two cases corresponds to the residual angle measured in ring shear tests and reported in the reference papers.

There is no available experimental data regarding the variation of the friction angle with the velocity in the two analyzed landslides. The strain hardening introduced is indicated in Figure 18 inspired in experimental tests (Wang et al., 2010 and Wedage et al., 1998a). Besides, the maximum values of friction angles and the values of the parameter controlling the strength increase variation, χ, were defined taking into account the condition of fitting the measured accumulated displacement.

The obtained results are indicated in Figure 19 and Figure 20. The agreement is reasonably good. The peak acceleration measured in January 1991 in Alverà slide is poorly reproduced by the model. The computational model is capable of interpreting the evolution of the landslide motion induced by changes in external action and the resistant forces. The velocity increment registered

in 01/91 cannot be correlated with an increase of the water level (notice that the water level at this period did not increase significantly compared with the rest of values) and the velocity reached a maximum of 12 mm/day. This circumstance cannot be reproduced by the computational model.

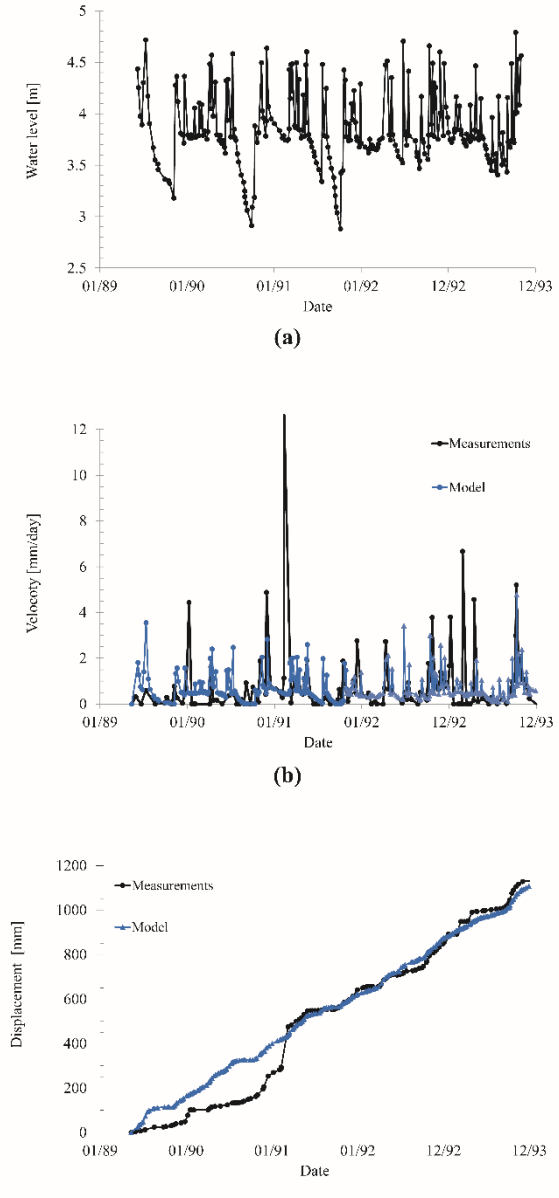

Figure 19. Measured and computed values of (a) height of the water level; (b) slide velocity; and (c) accumulated displacement in case of Alverà slide.

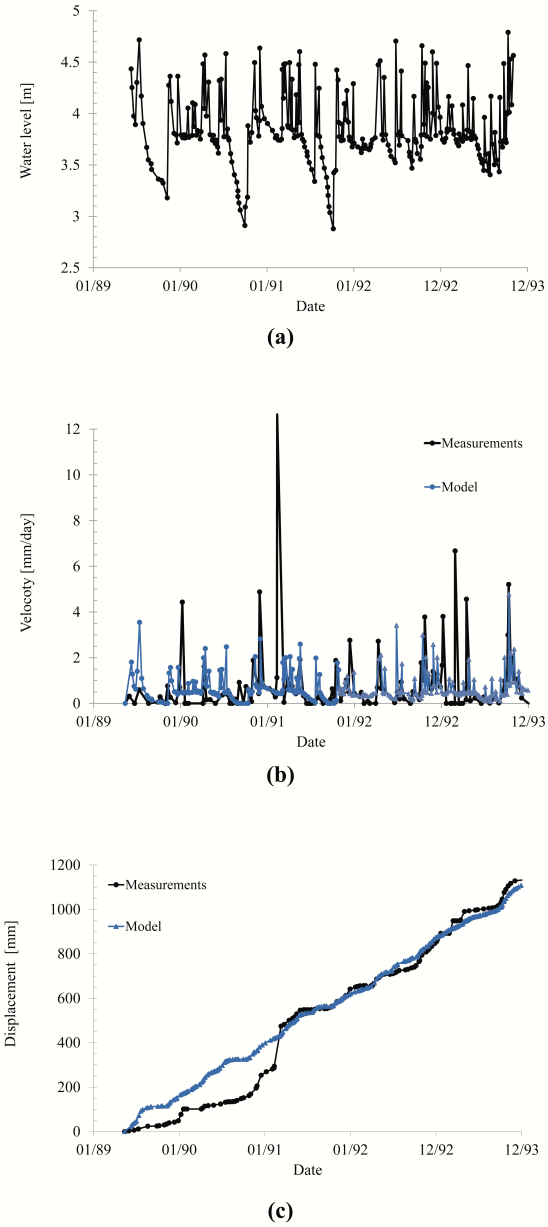

Figure 20. Measured and computed values of (a) height of the water level; (b) slide velocity; and (c) accumulated displacement in case of Vallcebre landslide.

3.2.2 From creeping to accelerated motion

Frictional heating of the slip zone can explain the large runout and velocity of some landslides. Vajont landslide is a good example. As discussed in Section 3.1.1, degradation, implemented as strain-softening, is not enough to reproduce such a fast motion and a very large run-out. The methodology applied to analyse Vajont landslide which includes thermal pressurization (Pinyol and Alonso, 2010) was also used to evaluate the

potential acceleration of an incipient large landslide reactivated by a rapid drawdown: Canelles landslide (Spain) (Pinyol et al., 2016). A long crack, 30 cm wide as a maximum, marked the boundary of a large translational landslide, 40 Mm^3. The unstable rock mass on the left margin of Canelles reservoir is a sequence of folded limestone and sandstone layers. The sliding surface was located in a continuous and relatively thin high plasticity clay layer. Pinyol et al. (2012) describe a THM analysis of this landslide, represented in 2D, by two interacting blocks. The computed results indicate that the thermal effect could induce the acceleration of the mobilized mass.

Later on, the case was revisited and the post-failure response was simulated by a MPM code able to deal with non-isothermal problems and the dissipation of the frictional work into heat (Alvarado et al., 2019).

This continuum THM analysis concluded that the landslide could accelerate and reach a maximum velocity of 8 m/s. Figure 22 shows the computed results at the end of the motion in terms of displacement, deviatoric plastic strains, temperature increment during motion and pore water pressure. The permeability of the clay layer, where the pre-existing sliding surface was located, is low enough for the accumulation of thermally-induced excess pore water pressure which leads to the loss of the effective frictional strength and the acceleration of the mass. Notice that temperature increments are computed along the shear bands. In the internal shearing bands developed within the mobilized mass, the temperature increases around 10º. Due to the relatively high permeability of the fissured and degraded banks of siltstones and limestones, the thermal-induced excess pore water pressure generated during motion has not been included in the mobilized rock mass.

According to the results, the velocity increases up to 1.44 m/s in 5 seconds. At a certain moment, the sliding velocity reduces due to the transfer of sliding mass to more stable positions in the lower part of the landslide. In addition, the weight reduction over the steeper upper part of the sliding surface. The slope becomes stable after 55 m of run-out

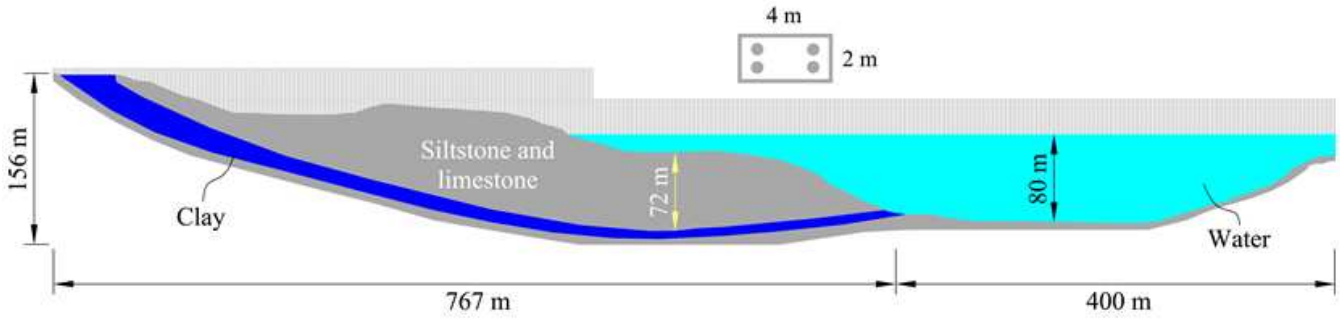

Figure 21. MPM cross-section of Canelles landslide.

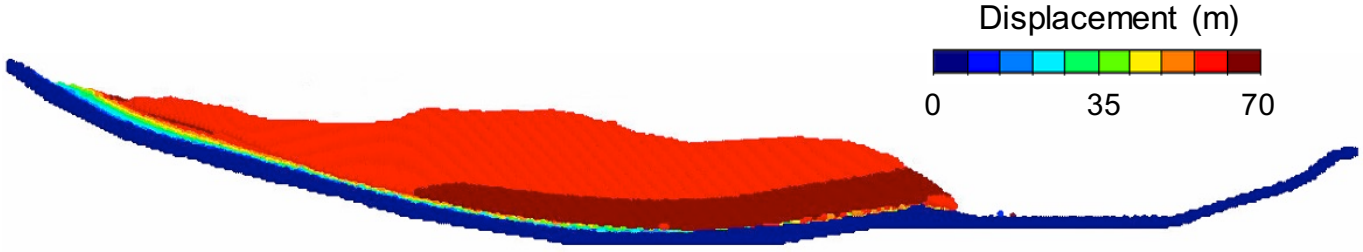

(a)

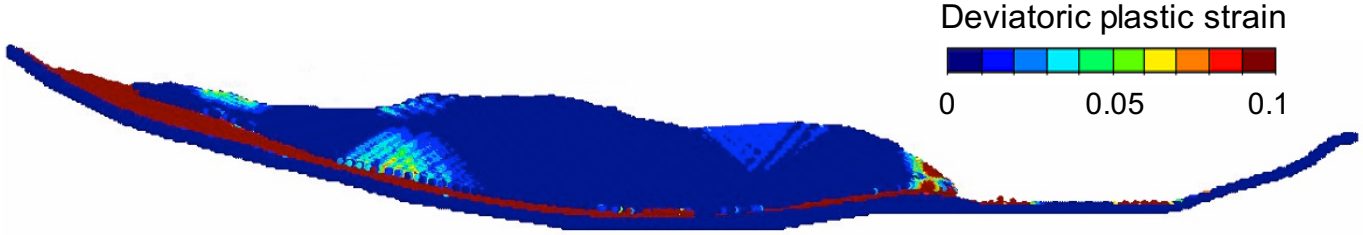

(b)

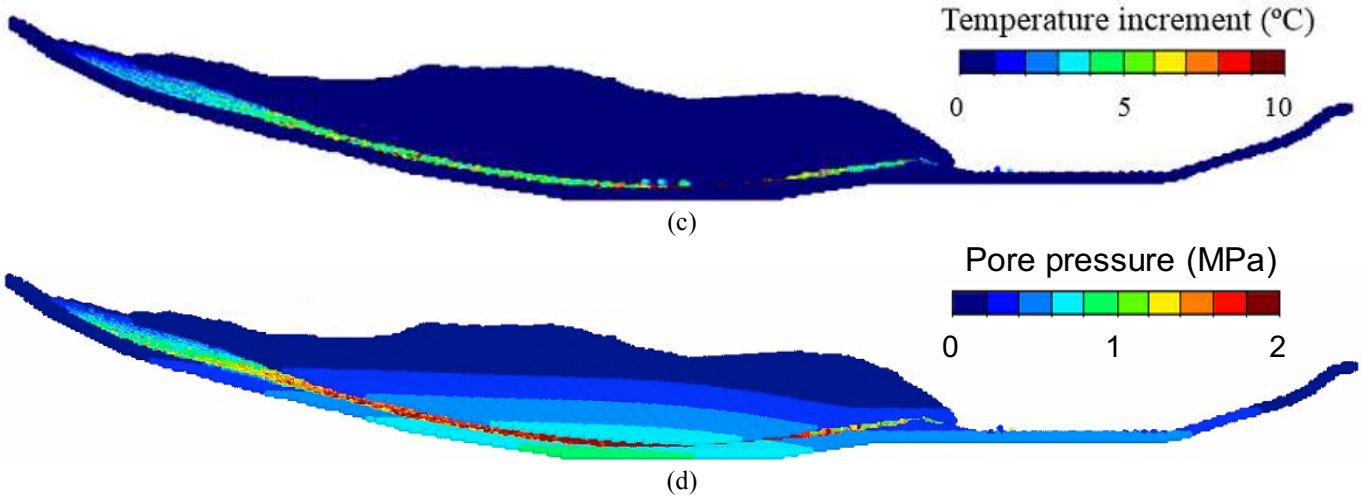

Figure 22. Calculated results of the THM analysis of Canelles landslide at the end of the motion.

These results showed the potential acceleration of Canelles landslide. However, they are not consistent with the observed behavior. Canelles landslide never accelerated.

The strain-rate effect discussed in the previous section that is able to prevent the acceleration of planar landslides is included in the analysis of Canelles landslide to explain the initial very small displacement. To do that, the strain- and strain rate dependent law given in Equation (19) was implemented in the constitutive Mohr-Coulomb model. This is an extension of Equation (13) to include strain rate effects on the friction angle, now expressed in terms of friction angle because of numerical facilities.

Table 2. Material parameters for the case of Canelles landslide.

Parameters	Symbol	Value	Units
Clay Soil			
Porosity	n	0.2	-
Permeability	k	1.00E-8	m/s
Young's Modulus	E	500	MPa
Poisson's ratio	ν	0.3	-
Residual friction	ϕ'_{res}	11.5	◦
Parameter strain softening	η	50	-
Shear band thickness	e	2	cm
Parameters strain rate effects	$\bar{\phi}$	2	◦
	α	10^7	1/s
Siltstones and limestone			
Porosity	n	0.3	-
Permeability	k	1.00E-6	m/s
Young's Modulus	E	2500	MPa
Poisson's ratio	ν	0.3	-
Effective cohesion, Peak, residual	c'_p / c'_{res}	1000/500	kPa
Effective friction. Peak, residual	ϕ'_p / ϕ'_{res}	35/32	◦
Shear band thickness	e	10	cm

$$\phi' = \phi'_{res} + \left(\phi'_{peak} - \phi'_{res}\right) e^{-\eta \varepsilon_d^p} + \bar{\phi}' \left(1 - e^{-\alpha \varepsilon_d^p}\right) \qquad (19)$$

ϕ'_{peak} and ϕ'_{res} are the maximum and minimum effective friction angle associated with shearing at a slow strain rate which describes the strength-softening strain-rate independent. η is a model parameter that controls this strain softening. $\bar{\phi}'$ is the maximum increment of the effective friction angle due to rate effects, and α is the parameter controlling the rate strain effects. ε_d^p is the deviatoric plastic strain and ε_d^p is the deviatoric plastic strain rate.

The strain-softening law (Eq. 19) characterizes the mobilized rock above the sliding surface without including strain rate effects. The estimated peak and residual values are indicated in Table 2. These values were selected taking into account the properties of rock layers described in the geological analysis carried out in Pinyol et al. (2012).

On the contrary, the clayey layer is at residual condition and the strain-softening is not included. A strain rate hardening, providing a moderate maximum increase in residual friction ($\bar{\phi}' = 2°$) and a value $\alpha = 10^7$ (1/s) were adopted. These

values are consistent with the correlation between the increase of shear strength and the plasticity index presented by Wedage et al. (1998a) based on tests on clays and clay shales.

In order to highlight the effect of phenomena included in the analysis, we evaluated four cases:

- Case 1: Thermal interaction allowed; no strain-rate hardening.
- Case 2: Thermal interaction allowed; strain-rate hardening activated.
- Case 3: No thermal interaction; no strain-rate hardening.
- Case 4: No thermal interaction; strain-rate hardening activated.

Figure 23 shows the computed displacements for each case. Case 1 corresponds to the previous hypothesis in which the thermal interaction leads to the acceleration of the landslide. When strain rate hardening is included (Case 2) the motion becomes totally different. The additional frictional strength (2º) prevent the thermal-induced acceleration and the velocity remains small enough to avoid the drop of the frictional strength. It results in a maximum displacement of the toe of the slope of 6 cm.

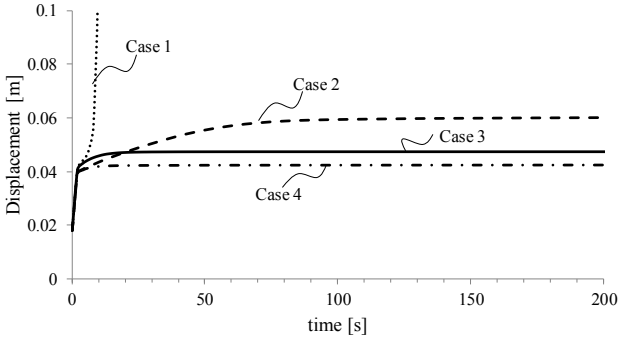

Figure 23. Computed displacements of Canelles landslide for different hypothesis of calculation.

Cases 3 and 4 do not include thermal interaction. Comparing this cases with Case 2, it is observed that the final displacement in Case 2 is is larger than the values calculated for the isothermal case (Cases 3 and 4) because of the development of (low) heat induced excess pore pressures in the sliding surface, even if the sliding velocity remains within a creeping stage. Therefore, the thermal interaction has an effect on the creeping velocity especially for low permeability materials. This conclusion, which was also noticed in the analysis reported in Alonso et al. (2016) for simple geometries involving one-dimensional conditions, is also found in the continuous MPM solution for a realistic geometry, based on a real case.

3.2.3 Earthquake-triggered landslides

Earthquake-induced landslides often exhibit long run-out and reach high velocities. Most of these landslides are reactivated motions and the shear zones are at residual strength conditions. An example is the Tsaoling landslide, the largest and best-documented case triggered by the 1999 Taiwan Chi-Chi earthquake (Mw=7.6) (Schulz and Wang, 2014). It mobilized a 140 m thick of almost planar slide constituted by very flat bedding planes within alternated fine sandstone and shale beds dipping 14º. The average speed of the landslide motion was around 35 m/s and it traveled more than 2500 m crossing the valley and hitting the opposite slope of the valley where it reached a height of 60 m height (Yang et al., 2014; Wu and Chen, 2011).

As discussed in Yang et al. (2014), peak and residual strength envelopes obtained using traditional direct shear tests at low slip rates cannot explain the failure and post-failure response of the landslide subjected to Chi-Chi earthquake. The peak and residual strength measured are 39º and 23º, respectively (Lee, 2001; Towhata et al., 2001). Newmark's analysis (Newmark, 1965) of this landslide assuming a constant strength conclude that the landslide motion stops when seismic ground motion finishes because the residual friction angle (23º) is greater than the dipping angle of the slope (14º) and the available residual strength is capable of compensating the inertial terms of the motion.

Dong et al. (2003), Yang et al. (2014) and Chen et al. (2014) reproduce successfully the final runout by means a Newmark's analysis when including displacement and velocity-dependent frictional laws, such as Equation (11) and (12). They calibrated the laws with rotatory shear test results.

Continuum numerical models developed to analyzed Tsaoling landslide, such as the hydraulic flow analysis (Kuo et al., 2009), the particle flow approach (PFC2D) (Tang et al., 2009) and the discontinuous deformation analysis (DDA) (Wu

and Chen, 2011) require an initial relatively high friction angle to explain the stable initial situation and the subsequent strength weakening during the motion. Otherwise, it was not possible to reproduce the landslide velocity and run-out. In particular, Wi and Chen (2011) dropped the strength to zero cohesion and zero friction angle.

In all of these analyses, a drop of strength until very low values (friction coefficient lower than 0.1, equivalent to friction angles lower than 6º) is imposed ad-hoc without explicitly including any physical phenomena causing such a decrease.

In the following, the motion of earthquake-induced landslides is evaluated. First, Newmark's analysis for planar landslides is presented including a velocity-dependent shear strength envelope. This feature is combined later with thermal effects for simple geometries of slope analysed in MPM.

Newmark's method is applied considering the influence of non-constant shear strength (as discussed in Lemos and Coelho, 1991). The method consists in computing the accumulated displacement, induced by an earthquake, of a block that slides on an inclined plane, representing a planar landslide.

Consider the planar landslide shown in Figure 24. A parallel water level is imposed at h_w. The force F represents the earthquake action whose direction is assumed constant and defined by an angle α with respect to the slope inclination. F is expressed in terms of a coefficient $k(t)$ which varies in time:

$$F = k(t)W \tag{20}$$

where W is the weight of the mobilized mass.

The dynamic equation of equilibrium governing the motion is:

$$\tan\beta + \left(\frac{\gamma_w h_w}{\gamma_s D} - 1\right)\tan\phi' + k\frac{\sin\alpha}{\cos\beta}\tan\phi' + k\frac{\cos\alpha}{\cos\beta} = \frac{a}{g\cos\beta} \tag{21}$$

where γ_w and γ_s is the specific weight of water and soil, respectively, g the gravity acceleration and a the acceleration of the mobilized mass. The resistance of the soil along the sliding surface was defined by Mohr-Coulomb law with nil cohesion (residual condition). Notice that Equation (21) assumes that the sliding mass never losses contact with the stable mass of the slope.

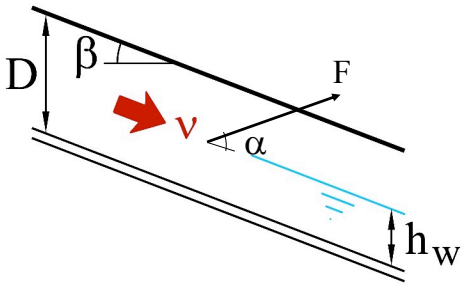

Figure 24. Schematic representation of a planar landslide subjected to a seismic action.

The critical acceleration (minimum value of $k(t)$) required to trigger the motion, results from imposing limit equilibrium (a=0 in Equation (21)):

$$k^{critical} = \frac{\tan\phi'\left(1 - \frac{\gamma_w h_w}{\gamma_s D}\right) - \tan\beta}{\left(\frac{\sin\alpha}{\cos\beta}\tan\phi' + \frac{\cos\alpha}{\cos\beta}\right)} \tag{22}$$

For k values higher than $k^{critical}$, the landslide acceleration is equal to:

$$\frac{a}{g\cos\beta} = \left(\frac{\sin\alpha}{\cos\beta}\tan\phi' + \frac{\cos\alpha}{\cos\beta}\right)\left(k - k^{critica}\right) \tag{23}$$

This acceleration can be integrated in time to obtain the velocity- and displacement-time history. The method takes into account that only acceleration values exceeding the critical seismic acceleration can trigger the motion and, assuming that upslope resistance to sliding is infinitely large. In other words, the upslope displacements are prohibited.

This procedure is applied for the following data: D = 30m, α = 15º; β = 15º and an earthquake characterized by the acceleration-time history shown in Figure 26.

The non-constant friction angle law of Equation (8) is considered. The minimum friction angle is equal to 17º and h_w = 5.5 m. For these conditions, the initial safety factor of the slope, before the application of the earthquake, is $FS_{initial}$=1.04 (defined with respect to the minimum angle associated to the rest state).

Without shear strain rate effects (constant friction angle) the maximum Newmark's displacement is equal to 1.840 m (Figure 26).

Increasing of shear strength with velocity leads, obviously, to smaller values of accumulated displacement to 2.5 m. Figure 26 also shows the accumulated displacement for a strain rate hardening plotted in Figure 27 (ϕ_{max}=19º and χ =10 s/m). The strength increment provided during motion is able to reduce the maximum accumulated displacement. The triggering of the slide depends on the minimum strength associated with the resting state. During motion, the critical strength varies due to the slide velocity. The critical value of the acceleration in time for the case of non-constant strength is plotted in Figure 26.

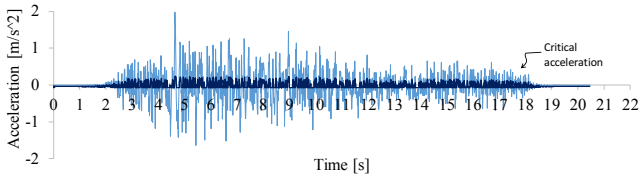

Figure 25. Seismogram applied in the seismic analyses and critical acceleration of the case of planar landslide and strain-rate hardening

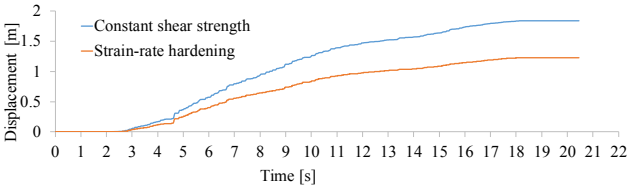

(a)

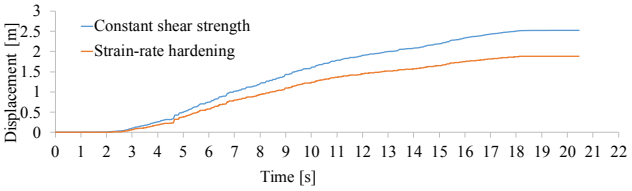

(b)

Figure 26. Planar landslide. Computed Newmark's displacement for constant and strain rate hardening. Initial safety factor associated with the friction angle in resting state (a) $SF_{initial}$ = 1.04; (b) $SF_{initial}$ = 0.95.

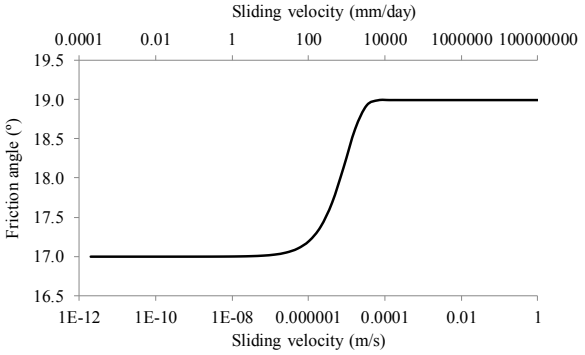

Figure 27. Velocity-dependent friction angle law introduced in the Newmark's analysis of planar landslide.

Considerer now an extreme case in which the slide is initially creeping at constant velocity. This situation is reached for h_w=10 m. This situation has a safety factor with respect to the minimum value of friction angle of $FS_{initial}$=0.95. Thanks to the strain-rate hardening (Figure 27) and according to Equation (17) and (18), the planar landslide moves at constant velocity equal to 0.45 mm/day. The application of the earthquake of Figure 26 induced the accumulation of 1.9 m of runout (Figure 26b). Without the positive effect of the strain rate, the accumulated displacement increases up to 2.6m.

Even in this case, the earthquake is not able to induce the acceleration of the landslide after the ground motion stops. Once seismic action ends, the equilibrium conditions (at rest of creeping motion) end up being restored.

As previously discussed, thermal effects induced by the dissipation of frictional work along the sliding surfaces might explain the catastrophic acceleration also in the case of earthquake-induced landslide. This effect is included in the following analysis carried out in the THM-MPM code. The homogeneous slope of Figure 28 is modelled with mesh element and materials points also indicated in the figure. The thermal properties of the liquid and solid particles are the same used in the previous THM analysis (Table 1). The mechanical properties assigned to the soil are indicated in Table 3. Equation (19) defines the strain- and strain-rate dependent strength. Strain softening is applied in this case, although the discussion focusses in the strain rate effects. The parameters defined leads to an increment of friction angle from the residual to the maximum value associated when the equivalent plastic strain rate increases from 10^{-7} to $5 \cdot 10^{-5}$ 1/s (which corresponds, taking into account the shear band thickness, to values of velocity ranging from $5 \cdot 10^{-4}$ to $3 \cdot 10^{-2}$ mm/min). Initially, the slope is saturated assuming the position of the water level on the surface. For simplicity, the initial stationary water flow and pressure distribution are not calculated. The initial effective stress is calculated with the submerged specific weight. The THM calculation allows the excess pore water pressure generated due to thermal interaction.

The same earthquake used in the previous analysis for planar landslides, whose acceleration in time is plotted in Figure 25, is also applied to

the slope. It is modelled by imposing the velocity of the material points located in the elements of the bottom of the model corresponding to the integration of the earthquake acceleration. On the lateral contours, absorbing boundaries are applied in order to simulate an extended model in which the waves are dissipated.

The initial safety factor of the slope computed by means of limit equilibrium (Slide program, version 2018, Rocscience Inc.), for a constant Mohr-Coulomb strength, is equal to SF=1.58 and SF=1.102 for peak and residual values of the strength envelope, respectively. Notice that the strain softening is only attributed to the cohesion.

Figure 29 shows the evolution of the horizontal displacement of the toe of the slope (run-out) in time and Figure 30 shows the contour of final displacements for the simulations. At time 0, once the slope is built, the earthquake was applied. Consider first the case in which only the strain softening for the cohesion was included (Base case). The computed results in terms of the final calculated run-out (0.82 m) can be compared with the values computed by means of Newmark's method for circular surfaces using Slide program (version 2018, Rocscience Inc.). The maximum value of the displacement according to this method is equal to 1.14 m for the case of residual cohesion. However, Figure 30a shows larger displacements in the top of the slope for this case.

In a second case which includes strain rate hardening, the increment of the strength with the velocity leads to prevent the acceleration of the landslide. The run-out reduced to 5 cm but there are larger displacements in the top of the slope. For the third case, thermal coupling was considered without strain rate hardening. The final displacement increased to more than 12 m as shown in Figure 30c due to the thermal-induced excess pore water pressure that is generated during motion, which essentially does not dissipate because of the low permeability of the material. The calculated run-out for this hypothesis was 11.5 m and reduced to 8.75 m in the fourth case, when strain rate hardening is included. The accumulated displacement reduced to 9 m. This smaller displacement is consistent with the lower temperature and excess pore pressure generated during the motion in comparison with the case without rate effects as shown in Figure 31.

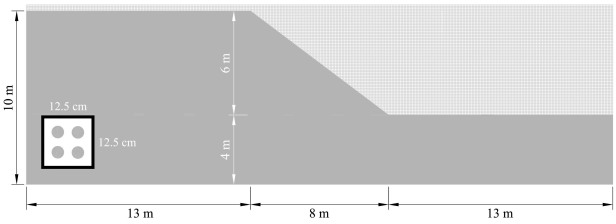

Figure 28. MPM mesh discretization.

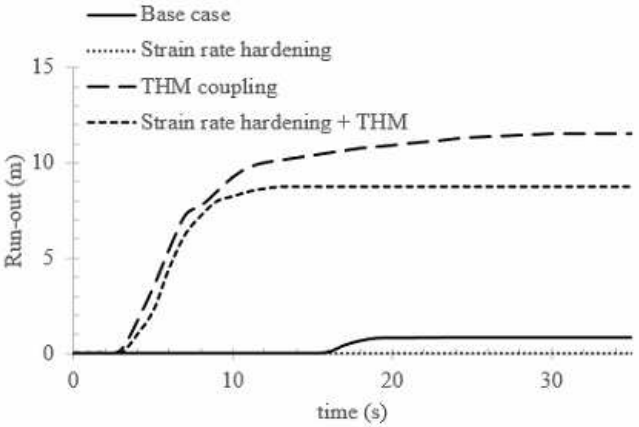

Figure 29. Earthquake induced run-out for different hypothesis.

Table 3. Material parameters for the case of slope subjected to earthquake analysed in MPM.

Parameters	Symbol	Value	Unit
Saturated density	ρ_w	2275	kg/m^3
Young modulus	E	20	MPa
Porosity	n	0.4	-
Effective friction. Peak, residual	ϕ'_p / ϕ'_{res}	38/38	º
Effective cohesion, Peak, residual	c'_p / c'_{res}	2.5/0.1	kPa
Poisson's ratio	ν	0.33	-
Permeability	k	$5 \cdot 10^{-11}$	m/s
Band thickness	e	1	cm
Strain softening parameter	η	500	-
Maximum increment of angle	$\overline{\phi}'$	2	º
Strain rate hardening parameter	α	10^5	1/s

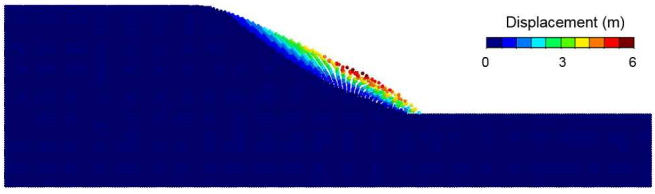

(a)

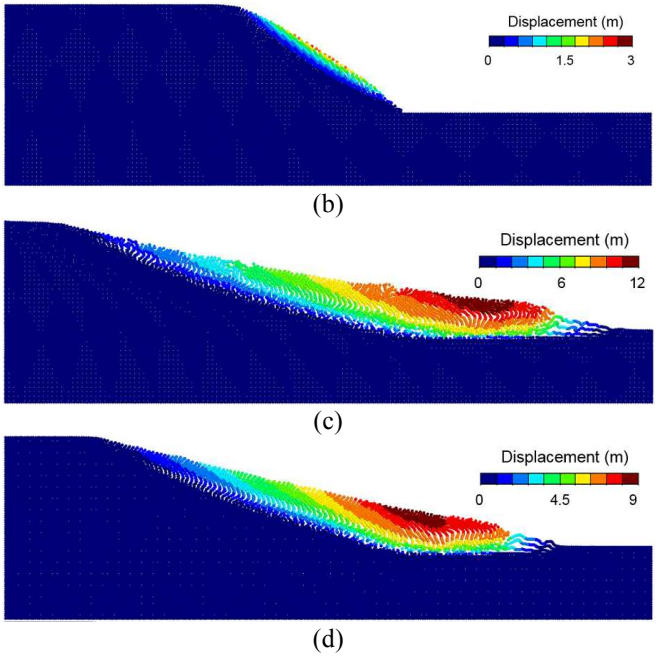

Figure 30. Computed displacement at the end of the motion of the slope subjected to an earthquake.

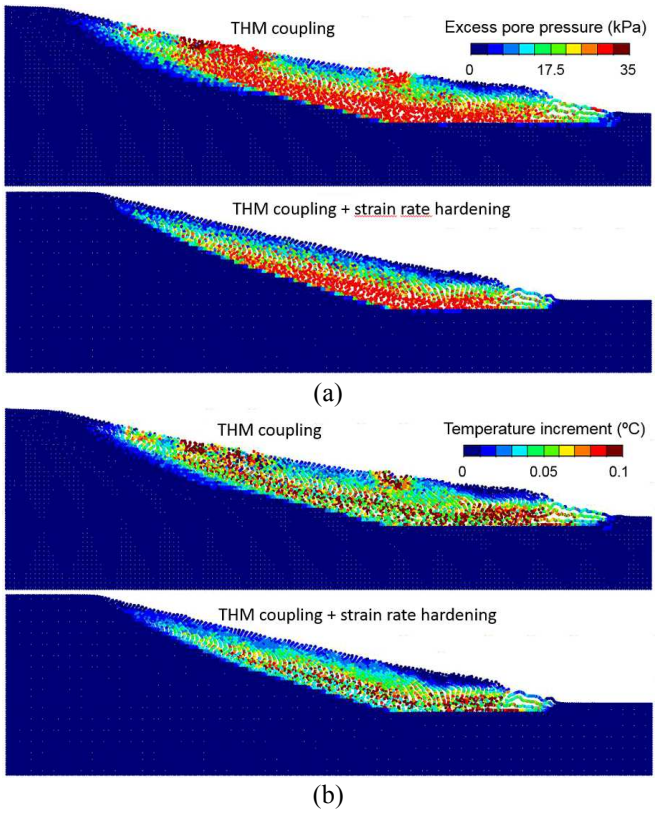

Figure 31. (a) Excess pore water pressure and (b) temperature increment calculated for the cases indicated.

4 CONCLUSIONS

As a general trend, the collected experimental results reported in the literature of shearing rate effect on fast residual strength indicate that there is a critical low value of velocity below which strain-rate effects are negligible or very small. The residual strength remains constant for displacement rate below this critical low value that, for the tests evaluated, is around 1 mm/min to 100 mm/min. Although an exhaustive analysis has not been carried out in this article, it is known that this value is not constant and depends, for a given soil, on the normal stress.

For higher values of displacement rate than the critical low value, the strain rate effect becomes evident exhibiting positive, neutral or negative values depending on the material and testing conditions. The increase of the strength observed is associated with changes in the structure of the shear band at particle level because of the disordering of clay particles. This phenomenon is understood in this article as an intrinsic frictional feature of soils which determine the residual strength. In this sense, the strength is assumed to be a strain rate dependent property.

In the shearing tests evaluated, the applied displacement rates range from 10^{-5} mm/min to 10^{4} mm/min. These rates corresponds to a wide velocity range which varies between very slow and very rapid landslides. However, to extrapolate the observed behaviour at the laboratory to the field scale, we should take into account several additional factors, not only the shearing rate. In general, the accumulated displacement reached in the rapid ring shear tests reported in the literature is smaller than 1 m. This is a low value compared with the landslide displacement, especially in cases of moderate to fast landslides. At microstructural level the shear band structure reached at certain velocity during 1 m displacement, probably does not change with further displacement at same velocity. However, coupled phenomena, inducing excess pore water pressure or temperature changes, developed during motion, may be highly dependent on the accumulated displacement.

This article evaluates the phenomenon of thermal pressurization at the shear band level due to the dissipation in heat of the frictional work. The relevance of the thermo-hydro-mechanical effects on the discussed rapid shearing tests is

analysed employing an analytical solution for the excess pore water pressure generated during the test under adiabatic and undrained conditions. The results indicate that the THM effects may be relevant depending on the soil properties and the testing conditions. The shear band thickness, defined as imput parameter, has an important effect. Thermal induced excess pore water pressure is higher for thinner shear bands, which are typically associated with fine particles. Regarding testing conditions, since the excess pore water pressure is generated during motion, the maximum accumulated displacement reached during the test determines the thermal-induced drop of residual strength. For instance, even a very fast shearing, such as the tests reported by Tika et al. (1996) at a velocity of 2000 mm/min, leads to a residual strength drop equal to 12%, with respect to the slow drained shearing strength, when accumulated displacement reaches 150 mm (assuming a shear band thickness of 1mm). This effect actually can be even smaller due to the dissipation of water and the heat flow during the test.

Therefore, and according to theoretical results, THM effects inducing the loss of available effective strength may develop during fast shearing tests. Depending on the soil properties and testing conditions, they can be significant and can explain the observed negative effect. However, in other cases, the effect, not so significant, can be countered by hardening strain-rate effects associated with intrinsic soil properties. It may occur in fine soils in which the disordering of platy particles is notable and may have a significant positive effect that cannot be completely counteracted by thermal interaction.

THM effect will likely be significant in case of large accumulated displacements that typically take place in the field during landslide motion where the accumulated displacements are larger. This is discussed in this article by numerical modeling including heat flow and pore pressure dissipation.

Direct effect of temperature on the intrinsic property of soil residual strength is also discussed in the paper by referring to recent publications. Temperature changes are measured in shallow landslides. The behavior observed in the laboratory experiments is that the temperature effect is strain rate dependent. The available experimental data is limited.

The factors controlling the shear strength and their effect on landslide triggering and motion are evaluated through analytical and numerical analysis in the paper. The intrinsic factors determining the non-constant shear strength are included in a constitutive law which accounts for strain softening and strain rate hardening effects.

Strain-softening leads to progressive failure phenomena. The MPM modeling of the well-documented case of Selborne is described for discussion. Progressive failure phenomenon, which controls the developing of first failures, is also relevant in the case of ancient landslides due to the development of internal shearing during motion.

A sensitivity analysis on peak and residual strength expressed in terms of Bishop brittleness index (I_B) shows the strain-softening effects on the landslide triggering and run-out. The onset of failure depends on the magnitude of the triggering mechanism. The higher the intensity of the triggering mechanism, the lower I_B is sufficient to induce instability. This fact allows defining a brittleness threshold, which determines the minimum brittleness required to induce instability for a given triggering mechanism. Additionally, it was found that run-out increases with I_B. The softening acts of a mechanism of acceleration.

An exponential law is used to describe the strain-rate hardening. The law is defined in terms of a minimum and a maximum friction angle and the range of displacement-rate in which the strength varies between these two limits. This strain rate range in which this increment takes place is assumed constant. Therefore, the dependence with total stress of the critical low-velocity value, below which the strain rate effect is negligible, is not included.

The analytical simulation of two well-documented cases of creeping landslides, simplified as planar shows that the strain-rate hardening allows explaining the observed low velocity. In these cases, if a simple Mohr-Coulomb strength law were selected, the reported variation of the water level in the landslide would lead to unrealistic rapid velocities.

Finally, a landslide analysis is presented including thermal pore water pressure

pressurization combined with strain softening and strain-rate hardening. The first case analysed assesses the post-failure behavior of Canelles landslides. The THM-MPM analysis leads to the acceleration of the landslide. Then, it is demonstrated that positive strain rate effects may prevent the pore water pressure build-up and therefore the landslide does not accelerate catastrophically.

Strain rate effects and thermal interaction also compete in earthquake-induced landslides and determine the final run-out. The academic examples presented offer an explanation for the observed rapid acceleration in real cases in which liquefaction is discarded. Some discussions found in the literature explain this rapid acceleration of earthquake-induced landslides by including explicitly strong strength weakening in the shearing strength constitutive law without considering other coupled effects. The paper offers an alternative explanation.

5 REFERENCE LIST

Alonso, E. E., Pinyol, N. M., Puzrin, A. M. (2010). "*Geomechanics of Failures. Advanced topics*". Springer.

Alonso, E. E., Zervos, A., Pinyol, N. M. (2016). "*Thermo-poro-mechanical analysis of landslides: from creeping behaviour to catastrophic failure*." Géotechnique 66 (3), 202–219.

Alvarado, M., Pinyol, N. M, Alonso, (2009). "*Landslide motion assessment including rate effects and thermal interactions : revisiting the Canelles landslide*" Canadian Geotechnical Journal 56, 1338–50.

Angeli, M. G., Menotti, R. M., Pausto, A., Silvano, S. (1991). "*Landslide studies in the Eastern Dolomites Mountains, Italy.*" Proceedings of the 6th international Symposium on Landslide. New Zeland. Vol. 1, 275-282.

Angeli, M.-G., Gasparetto, P., Menotti, R.M., Pasuto, A., and Silvano, S. (1996). "*A visco-plastic model for slope analysis applied to a mudslide in Cortina d'Ampezzo, Italy.*" Quarterly Journal of Engineering Geology and Hydrogeology 29, 233–240.

Angeli, M.-G., Pasuto, A., Silvano, S. (1999). "*Toward the definition of slope instability behavior in the Alverà mudslide (Cortina d'Ampezzo, Italy)*". Geomorphology 30(1–2), 201–211.

Bishop, A. W. (1967). "Progressive failure-with special reference to the mechanism causing it." Proc Geotech. Conf., Oslo 2:142–50.

Bishop, A. W., Green, G. E., Garga, V. K., Andresen, A., Brown, J. D. (1971). "*A new ring shear apparatus and its application to the measurement of residual strength.*" Géotechnique 21(4), 273–328.

Bjerrum, L. (1967). "*Progressive failure in slopes in overconsolidated plastic clays and clay shales*." J. Soil Mech. Found. Div. 93, 3–49.

Bowden, F., Tabor, D. (1964). "*The friction and lubrication of solids*". New York, NY, USA: Oxford University Press.

Cascini, L., Cuomo, S., Pastor, M. Sorbino, G. (2010). "*Modeling of Rainfall-Induced Shallow Landslides of the Flow-Type*." Journal of Geotechnical and Geoenvironmental Engineering 136 (1): 85–98.

Cecinato, F., Zervos, A., Veveakis, E. (2011). "*A thermo-mechanical model for the catastrophic collapse of large landslides*". Int. J. Numer. Methods Eng., 1507–35.

Chandler, R. J. (1977). "*Back analysis techniques for slope stabilization works: A case record."* Géotechnique 27(4), 479–495.

Cooper, M. (1996). "*The progressive development of a failure slip surface in over-consolidated clay at Selborne, UK".* Proceedings of the 7th international symposium on landslides, Trondheim, Norway (ed. K. Senneset), Rotterdam, the Netherlands: Balkema, pp. 683–688.

Cooper, M. R., Bromhead, E. N., Petley, D. J., Grant, D. I. (1998). "*The Selbourne cutting stability experiment*". Géotechnique 48(1), 83–101.

Corominas, J., Moya, J., Ledesma, A, Lloret, A., Gili, J. A. (2005). "*Prediction of ground displacements and velocities from groundwater level changes at the Vallcebre landslide (Eastern Pyrenees, Spain).*" Landslides 2, No. 2, 83–96.

Cruden, D. M., Varnes, D. J. (1996). "*Landslide types and processes. In: Landslide: investigation and mitigation. Special Report 247.*" Transportation Research Board, Washington, 36–75.

Davis, R.O., Desai, C.S., and Smith, N.R. (1993). "*Stability of motions of translational landslides".* Journal of Geotechnical Engineering, 119(3): 420–432.

Deganutty, A., Gasparetto, P. (1991). "*Some aspects of a mudslide in Cortina, Italy.*" Proceedings of the 6th international Symposium on Landslide. New Zeland. Vol. 1, 373-378.

Fern, J., Rohe, A. Soga, K. Alonso, E.E. (2018). "*The Material Point Method for Geotechnical Engineering. A Practical Guide*". CRC Press. Taylor & Francis Group.

Gens, A., Alonso, E. E. (2006). "*Aznalcóllar dam failure. Part 2: stability conditions and failure.*" Géotechnique 56: 185-201

Glastonbury J, Fell R (2008). "*A decision analysis framework for the assessment of likely post-failure velocity of translational and compound natural rock slope landslides*". Can. Geotech J. 45(3), 329–350.

Goren, L., Aharonov, E. & Anders, M. H. (2010). "*The long runoutof the Heart Mountain landslide: heating, pressurization, andcarbonate decomposition*". J. Geophys. Res.: Solid Earth 115, No. B10, B10210

Goren, L., Aharonov, E. (2007). "*Long runout landslides: The roleof frictional heating and hydraulic diffusivity*". Geophys. Res. Lett. 34(7), L07301.

Goren, L., Aharonov, E. (2009). "*On the stability of landslides: a thermo-poro-elastic approach*". Earth Planet. Sci. Lett. 277 (3–4), 365–372.

Habib, P. (1967). "*Sur un mode de glissement des massifs rocheux*" C R Acad Sc Paris. 264 (Serie A), 151-153 (In French).

He, S. M., Liu, W., Wang, J. (2015). "*Dynamic simulation of landslide based on thermo-poro-elastic approach*". Comput. Geosci.. 75,24–32.

Hisatsune, T., M. Okawara, and T. Mitachi (2009b), "*Measurement of frictional force and viscosity of high-purity montmorillonite by AFM".* Clay Sci., 14(3), 117–125.

Hungr, O., Leroueil, S., Picarelli, L. (2014). "*The Varnes classification of landslide types, an update*". Landslides 11, (2), 167–194.

Hungr, O., S. G. Evans, M. J. Bovis, and J.N. Hutchinson. (2001). "*Review of the Classification of Landslides of the Flow Type.*" Environmental and Engineering Geoscience 7 (3): 1–18. https://doi.org/10.2113/gseegeosci.7.3.221.

Kenney, T. C. (1967). "*The influence of mineral composition on the residual strength of natural soils*". Proceedings of geotechnical conference, Oslo, vol.1, pp. 123-129. Oslo: Norwegian Geotechnical Institute.

Kuo, C.Y., Tai, Y.C., Bouchut, F., Mangeney, A., Pelanti, M., Chen, R.F., Chang, K.J. (2009). "*Simulation of Tsaoling landslide, Taiwan, based on Saint Venant equations over general topography*". Engineering Geology 104, 181–189.

La Gatta, D. P. (1970). "*Residual strength of clays and clay shales by rotation shear tests*". Harvard Soil Mechanics Series, No. 86, Cambridge.

La Gatta, D. P. (1971). "*The effect of rate of displacement on measuring the residual strength of clay*". Contract report 5-71-5. Vicksburg: US Army Waterways Experiment Station.

Lemos L J., Coelho P. A. L. F. (1991) "*Displacements of Slopes Under Earthquake Loading.*" In: International conferences on Recent Advances in Geotechnical earthquake Engineering and Soil Dynamics. p. 1051–6.

Lemos, L. J. L. (1986). "*The effect of rate on the residual strength of soil*". PhD thesis, University of London.

Leroueil, S. (2001). "Natural slopes and cuts: Movement and failure mechanisms". Géotechnique 51(3), 197-243.

Lupini, J. F., Skinner, A. E. & Vaughan, P. R. (1981). "*The drained residual strength of cohesive soils*". Géotechnique 31, No. 2, 181-213.

Mesri, G. and Cepeda-Diaz, F. (1986). "*Residual shear strength of clays and shales.*" Géotechnique, 36(2), 269–274.

Mitchell, J.K. (1976). "*Fundamentals of soil behaviour*". New York: John Wiley & Sons.

Moore, R. (1991). "*The chemical and mineralogical controls upon the residual strength of pure and natural clays.*" Géotechnique 41(1), 35-47.

Newmark, N. M. (1940) "*Effects of earthquakes on dams and embankments*". Géotechnique 15 (2), 139–60.

Newmark, N.M. (1965), "*Effects of earthquakes on dams and embankments*", Géotechnique, Vol. 15, No. 2, pp. 139-160.

Ng, C. W. W. (2009. "*What is static liquefaction failure of loose fill slope*". The 1st Italian Workshop on Landslides, Napoli, Italy, Vol 1: 91-102.

Palmer, C., Rice, J. R. (1973) "*The growth of slip surfaces in the progressive failure of overconsolidated clay.*" Proc. Royal Society. 332, 527–48.

Panizza, M., Pasuto, A., Silvano, S., and Soldati, M. (1996). "*Tem- poral occurrence and activity of landslides in the area of Cortina d'Ampezzo (Dolomites, Italy)".* Geomorphology, 15: 311–326

Picarelli, L., L. Olivares, L. Comegna, and E. Damiano (2008). "*Mechanical Aspects of Flow-like Movements in Granular and Fine Grained Soils*". Rock Mechanics and Rock Engineering 41 (1): 179–97.

Pinyol, N. M., Alonso, E. E. (2010). "*Criteria for rapid sliding II. Thermo-hydro-mechanical and scale effect in Vaiont case*". Eng. Geol. 114 (3-4), 211–27.

Pinyol, N. M., Alonso, E. E., Corominas, J., Moya, J. (2012). "*Canelles landslide: modelling rapid drawdown and fast potential sliding*". Landslides 17 (1), 33–51.

Pinyol, N. M., Alonso, E. E., Corominas, J., Moya, J. (2016). "*Discussion on "Large landslides associated with a diapiric fold in Canelles reservoir (Spanish Pyrenees): Detailed geological – geomorphological mapping, trenching and electrical resistivity imaging*" by Gutiérrez et al. (2015)". Geomorphology. 263:170–4.

Pinyol, N.M., Alvarado, M., Alonso, E. E., Zabala, F. (2018). "*Thermal effects in landslide mobility*". Géotechnique 68(6), 528–46.

Potts, D. M., Dounias, G. T., Vaughan, P. R. (1990). "*Finite element analysis of progressive failure of Carsington embankment.*" Géotechnique 40: 79–101.

Potts, D., Kovacevic, N., Vaughan, P. (1997). "*Delayed collapse of cut slopes in stiff clay.*" Géotechnique 47, 953–82.

Puzrin, A. M., Germanovich, L. N. (2005). "*The growth of shear bands in the catastrophic failure of soils*." Proc. R. Soc. A. Math. Phys. Eng. Sci. 461: 1199–228.

Ramiah, B. K., Davalu, N. K. & Purushothamaraj, P. (1970). "*Influence of chemicals on residual strength of silty clay*". Soils Fdns 10, No. 1, 25-36.

Rice, J. R. (2001). "*New perspectives in crack and fault dynamics. Mechanics for a New Millennium*". Proceedings of the 20th international congress of theoretical and applied mechanics (eds H. Aref and J.W. Phillips), pp. 1–23. Chicago, IL, USA: Kluwer Academic Publishers.

Ruina, A., (1983). "*Slip instability and state variable friction laws*". J. Geophys. Res. 8(B12), 10359–10370.

Salt, G. (1988). "*Landslide mobility and remedial measures*". Proc. 5th Int. Symp. Landslides, Lausanne1, 757-762.

Sassa, K. 2000. "*Mechanism of Flows in Granular Soils.*" In GeoEng2000, 1671–1702. Melbourne, Australia: International Society for Rock Mechanics and Rock Engineering.

Scaringi, G., Hu, W., Xu, Q. (2018) "*Discussion on: "Experimental study of residual strength and the index of shear strength characteristics of clay soil*" [Eng. Geo. 233: 183 – 190]". Engineering Geology 242, 218–21.

Scaringi, G., Hu, W., Xu, Q., Huang, R. (2018). "*Shear-rate-dependent behavior of clayey bimaterial interfaces at landslide stress levels.*" Geophysical Research Letters 45, 766–777.

Scaringi, G., Maio, C. Di. (2016) "*Influence of displacement rate on residual shear strength of clays.*" Procedia Earth Planet Science 16, 137–45.

Schulz, W. H., Wang, G. (2014) "*Residual shear strength variability as a primary control on movement of landslides reactivated by earthquake-induced ground motion: Implications for coastal Oregon, U.S.*" J. Geophys. Res. Earth Surf. 119, 1617–1635.

Shibasaki, T., Matsuura, S., Okamoto, T. (2016) "*Experimental evidence for shallow, slow-moving landslides activated by a decrease in ground temperature*". Geophysical Research Letter 43, 6975–6984.

Shibasaki, T., S. Matsuura, S., Hasegawa, Y. (2017) "*Temperature- dependent residual shear strength characteristics of smectite-bearing landslide soils*" J. Geophys. Res. Solid Earth 122, 1449–1469.

Skempton, A. W. (1964) "*Fourth Rankine lecture: long-term stability of clay slopes.*" Géotechnique 14, 77–102.

Soga K., Alonso E., Yerro A., Kumar K., Bandara S., 2016. "*Trends in large-deformation analysis of landslide mass movements with particular emphasis on the material point method.*" Géotechnique 66(3), pp. 248-273.

Song, Y., Huang, D., Cen, D. (2016) "*Numerical modelling of the 2008 Wenchuan earthquake-triggered Daguangbao landslide using a velocity and displacement dependent friction law.*" Enginering Geololgy 215: 50–68.

Stark, T. D., and Eid, H. T. (1994). ''*Drained residual strength of cohesive soils.*'' J. Geotech. Eng. 120(5), 856–871

Stark, T. D., and Eid, H. T. (1997). "*Slope stability analyses in stiff fissured clays.*" J. Geotech. Geoenviron. Eng. 123(2), 335–343.

Stark, T. D., Eid, H.T. (1994) "*Slope stability analyses in stiff fissured clays.*" J. Geotech. Geoenviron. Eng.123, 335–43.

Stark, T. D., Hussain, M. (2013) "*Empirical Correlations: Drained Shear Strength for Slope Stability Analyses*." Journal of Geotechnical and Geoenvironmental Engineering 139, 853–62.

Sulsky, D., Chen, Z., Schreyer, H.L. (1994) "*A particle method for history-dependent materials*". Comput. Methods Appl. Mech. Eng. 118(1–2), 179–96.

Tang, C.L., Hu, J.C., Lin, M.L., Angelier, J., Lu, C.Y., Chan, Y.C., Chu, H.T., 2009. "*The Tsaoling landslide triggered by the Chi-Chi earthquake, Taiwan: insights from a discrete element simulation"*. Engineering Geology 106, 1–19.

Taylor, D. W. (1948) "*Fundamentals of soil mechanics*". New York: Wiley.

Terzaghi, K., Peck R. (1948) "*Soil mechanics in engineering practice*". New York: Wiley.

Tika, T. E. (1989a). "T*he effect of rate of shear on the residual strength of soi*l". PhD thesis, University of London.

Tika, T. E. (1989b). "*Ring shear tests 4/89-11/89*". Internal report. London: Imperial College.

Tika, T. E., Vaughan, P. R. & Lemos, L. (1996). "*Fast shearing of pre-existing shear zones in soil*". Géotechnique 46, No. 2, 197–233

Tiwari, B., and Marui, H. (2005). "*A new method for the correlation of residual shear strength of the soil with mineralogical composition.*" J. Geotech. Geoenviron. Eng. 131(9), 1139–1150

Tiwari, B., Tuladhar, G. R., Marui, H. (2005). "*Variation in residual shear strength of the soil with the salinity of pore fluid*." J. Geotech. Geoenviron. Eng., 131(12), 1445–1456.

Togo, T. Shimamoto, T., Ma, S., & Hirose, T. (2011). "*High- velocity frictional behavior of longmenshan fault gouge from Hongkou outcrop and its implications for dynamic weakening of fault during the 2008 wenchuan earthquake*". Eathquake Science, 24, 267-281.

Togo, T., Ma, S.L., Hirose, T. (2009). "*High- velocity frictional of faults: a review and implication for landslide studies"*. The Next Generation of Research on Earthquake – induced Landslides: an international Conference in commemoration of 10th Anniversary of the Chi-Chi Earthquake, pp. 205-216.

Togo, T., Ma, S.L., Hirose, T. (2009). "*High-velocity friction of faults: a reviewand implication for landslide studies*". The Next Generation of Research on Earthquake-induced Land- slides: an International Conference in Commemoration of 10th Anniversary of the Chi–Chi Earthquake, pp. 205–216.

Toyota, H., Nakamura, K., Sugimoto, M., Sakai, N. (2009) "*Ring shear tests to evaluate strength parameters in various remoulded soils"*. Géotechnique 59(8) 649–59.

Uriel Romero, S., Molina, R. (1977). "*Kinematic aspects of Vaiont slide*". In: Proceedings of the 3rd international conference of the ISRMR. Denver, CO, USA: National Academy of Sciences 2B, 865–70.

Vardoulakis I. (2000). "*Catastrophic landslides due to frictional heating of the failure plane*". Mech Cohesive-frictional Mater. 5, No. 6, 443–67.

Vardoulakis I. (2002) "*Dynamic thermo-poro-mechanical analysis of catastrophic landslides*". Géotechnique 52, No. 3, 157–71.

Veveakis, E., Vardoulakis, I., Di Toro, G. (2007). "*Thermoporomechanics of creeping landslides: The 1963 Vaiont slide, northern Italy*". J. Geophys. Res. 112, No. F3, F03026.

Voight, B., Faust, C. (1982). "*Frictional heat and strength loss in some rapid landslides*". Géotechnique 32, 43–54.

Wang, F. W., Sassa, K., and Wang, G. (2002). "*Mechanism of a long-runout landslide triggered by the August 1998 heavy rainfall in Fukushima Prefecture, Japan*". Eng. Geol. (Amsterdam), 63, 169–185.

Wang, G., Suemine, A., Schulz, W. H. (2010) "*Shear-rate-dependent strength control on the dynamics of rainfall-triggered landslides, Tokushima Prefecture, Japan*." Earth Surf Process Landforms 35(4), 407–16.

Wedage, A., Morgenstern, N. R. & Chan, D. H. (1998). "*A strain rate dependent constitutive model for clays at residual strength*". Can. Geotech. J. 35, No. 2, 364–373.

Wu, J.H., Chen, C.H., (2011). "*Application of DDA to simulate characteristics of the Tsaoling landslide*". Comput. Geotech. 38, 741-750.

Yang, C. et al., 2014. "*Initiation, movement, and run-out of the giant Tsaoling landslide — What can we learn from a simple rigid block model and a velocity – displacement dependent friction law?*" Engineering Geology 182,158–181.

Yerro A., Pinyol N. M., Alonso, E. (2016). "*Internal Progressive Failure in Deep- Seated landslides*". Rock Mechanics and Rock Engineering Volume 49, pages2317–2332.

Yerro, A., Pinyol, N. M., Alonso, E. E. (2015). "*Internal Progressive Failure in Deep-Seated Landslides*". Rock Mechanics and Rock Engineering 61 (9), .795–808.

Zabala, F., Rodari, R., Oldecop, L. (2004) "*Localización de deformaciones en estructuras utilizando el Método del Punto Material*". Revista Engenharia Estrutural 1290, No. 5400, 11–29 (in Spanish).